WCAP-10966 WESTINGHOUSE CLASS 3

ANC: A Westinghouse Advanced Nodal Computer Code

Y. S. Liu
A. Meliksetian
J. A. Rathkopf
D. C. Little
F. Nakano
M. J. Poploski

December 1985

Approved: _____
A. L. Casadei, Manager
Advanced Methods Development

Approved: _____
V. J. Esposito, Manager
Core Engineering

This work performed under shop order DGRF-20201

Westinghouse Electric Corporation
P. O. Box 3912
Pittsburgh, PA 15230

ABSTRACT

This report presents a description of the Westinghouse Advanced Nodal Code (ANC), which is a new version of the PALADON code. ANC incorporates three improvements to the PALADON code: (1) the nonlinear nodal expansion method, (2) the equivalence theory for cross section homogenization, and (3) a rod power recovery model. ANC and its related methodology were benchmarked against present design methods using the fine mesh diffusion model and measurements. The results presented in this report demonstrate that the ANC methodology is an accurate analytical tool that can be used for multidimensional nuclear analysis in the design and safety analyses of pressurized water reactor cores.

TABLE OF CONTENTS

ACKNOWLEDGMENTS

The authors wish to thank G. H. Minton, A. G. Cook, A. L. Casadei, and P. K. Doshi for their support during the course of this work. The assistance of D. L. Chapin, J. R. Secker, and K. W. Kopf is greatly appreciated.

LIST OF ILLUSTRATIONS

LIST OF ILLUSTRATIONS (cont)

LIST OF ILLUSTRATIONS (cont)

LIST OF TABLES

SECTION 1
INTRODUCTION

The PALADON topical report[1] submitted in April 1979 describes the calculational models used in the PALADON code and documents the qualification of PALADON for two-dimensional applications. Supplement 1 to the PALADON report,[2] submitted in September 1981, gives additional qualification data for the purpose of attaining approval to use PALADON for three-dimensional design applications. Specifically, Supplement 1 shows that PALADON can calculate the following in three dimensions under normal operating conditions: critical boron concentrations, control rod worths, reactivity coefficients, assembly average power and burnup distributions, assembly peak rod powers, $F_{xy}(z)$ peaking factors, and axial power shapes. For off-normal conditions, PALADON qualification data is given for steamline break and rod ejection calculations.

The PALADON report and its Supplement 1 give data which demonstrate the ability of the code to accurately predict assembly power, rod power, and reactivities. To improve this prediction accuracy and to eliminate the need to periodically benchmark PALADON calculations against more detailed calculations, a new nodal method has been incorporated into the PALADON code. The new version of the code, ANC (for Advanced Nodal Code), predicts reactivity and assembly and rod power distributions for normal and off-normal conditions, and it includes a nodal method that consists of three parts: (1) the nonlinear nodal expansion method, (2) a procedure for recovering rod power distribution, and (3) the equivalence theory for homogenization.

The objective of this topical report is to attain approval to use this new, advanced version of the PALADON code, ANC, for design. This report shows that ANC is an accurate method for core nuclear design, including the prediction of such design parameters as reactivity, assembly average power, rod power and flux, Doppler coefficients, moderator coefficients, boron worth, control rod

worth, burnable absorber worth, depletion, and other safety-related parameters. This report further shows that the conclusions given in the Nuclear Design portion of the reload methodology topical report[3] are valid when ANC is used for core nuclear design.

Section 2 of this report describes the improvements of the ANC code over the PALADON code. Subsection 2-1 details the Nodal Expansion Method (NEM), which is the first major improvement over PALADON. In NEM, the nodal coupling currents are obtained accurately by representing the neutron flux by the product of three fourth-order polynomials and by representing the feedback-induced cross section variation by the product of three second-order polynomials. The reflector can be modeled explicity or by albedo.

A new rod power recovery model is the second major improvement of the new nodal method. After completing the global nodal calculation, the intranodal rod power distribution can be recovered by superimposing a precalculated two-dimensional fine mesh power distribution on a form factor constructed from the global flux distribution. The form factors are constructed from
[

]a,c

Subsection 2-2 describes the rod power recovery method.

The third improvement incorporated in ANC is the simplified equivalence theory for generating homogenized cross sections. The procedure is described in subsection 2-3.

The level of accuracy of ANC is established in section 3, in which ANC calculations are compared with measured data and with results found by the discrete fine-mesh two-group diffusion code now used for core design.

SECTION 2
THEORY

2-1 NODAL THEORY

Modern nodal methods are characterized by rigorous expressions for the partial (or total) currents obtained by solving the two-group diffusion equations for each node. Methods for obtaining expressions for the partial currents include the analytical method, the one-dimensional Green's Function, the two-dimensional Green's Function, nodal expansion, and group theory. The nodal expansion method adopted in the Advanced Nodal Code offers two advantages over other methods: intranodal heterogeneity induced by burnup and feedback can be easily accounted for without rehomogenization, and the coupling coefficients are simple to calculate.

Subsection 2-1-1 describes the Nodal Expansion Method. A brief description of the various boundary conditions allowed in ANC is given in subsection 2-1-2. The nonlinear method used to account for the intranodal heterogeneity induced by burnup and feedback is presented in subsection 2-1-4.

2-1-1 Nodal Expansion Method

In the Nodal Expansion Method,[4] the spatial domain of a reactor core is divided into a set of contiguous rectangular parallelepipeds, called nodes. Their edges are perpendicular to the x-, y-, or z-axis. The average nodal flux and nodal surface currents are governed by the nodal balance equation and a set of auxilliary one-dimensional equations that couple average nodal flux to surface currents. In NEM, the auxilliary one-dimensional equations are obtained by approximating the one-dimensional flux by a polynomial expansion. The average nodal flux and nodal surface currents are found by solving these equations iteratively.

The nodal balance equation is obtained by integrating the two-group diffusion equation

$$\underline{\nabla} \cdot \underline{J}_g + \Sigma_{tg}\, \phi_g = \sum_{g'=1}^{2} \left[\left(\Sigma_{g'g} + \frac{\chi_g}{\lambda} \nu\Sigma_{fg'} \right) \phi_{g'} \right] , \quad g = 1, 2 \tag{2-1}$$

over the volume of a rectangular box, $V_m = a_x^m\, a_y^m\, a_z^m$:

$$\sum_{u=x,y,z} \frac{1}{a_u^m} \left[\left(J_{gul}^{out,m} + J_{gur}^{out,m} \right) - \left(J_{gul}^{in,m} + J_{gur}^{in,m} \right) \right]$$

$$+ \bar{\Sigma}_{tg}^{m}\, \bar{\phi}_g^m = \sum_{g'=1}^{2} \left(\bar{\Sigma}_{g'g}^{m} + \frac{\chi_g}{\lambda} \nu\bar{\Sigma}_{fg'}^{m} \right) \bar{\phi}_{g'}^{m} , \qquad \begin{array}{l} g = 1, 2 \\ l = \text{left} \\ r = \text{right} \end{array} \tag{2-2}$$

where

$\underline{J}_g$ = total current in group g

ϕ_g = scalar flux in group g

Σ_{tg} = total cross section for group g

$\Sigma_{g'g}$ = group g' to group g scattering cross section

χ_g = fraction of fission neutrons released in group g

λ = multiplication constant

ν = number of neutrons per fission

Σ_{fg} = fission cross section for group g

$$\bar{\phi}_g^m = \text{average nodal flux}$$

$$= \frac{1}{a_x^m \; a_y^m \; a_z^m} \int_0^{a_x^m} \int_0^{a_y^m} \int_0^{a_z^m} \phi_g(x,y,z)\, dx\, dy\, dz$$

$$\bar{\Sigma}_{\alpha g}^m = \frac{1}{\bar{\phi}_g^m} \int_{V_m} \phi_g \Sigma_{\alpha g}\, dV$$

and

$$\frac{1}{\bar{D}_g^m} = \frac{1}{\bar{\phi}_g^m} \int_{V_m} \phi_g \frac{1}{D_g}\, dV$$

The incoming and outgoing partial currents in group g, $J_{gul}^{in,m}$ and $J_{gul}^{out,m}$, respectively, are the averages over the left-hand surface of node m, perpendicular to direction u such that

$$J_{gul}^m = J_{gul}^{in,m} - J_{gul}^{out,m}$$

where the total current is defined as follows:

$$J_{gul}^m = \frac{1}{a_v^m \; a_w^m} \int_0^{a_v^m} \int_0^{a_w^m} J_{gu}(u = 0,v,w)\, dv\, dw$$

$$= \frac{1}{a_v^m \; a_w^m} \int_0^{a_v^m} \int_0^{a_w^m} - D_g(u = 0,v,w) \left[\frac{\partial}{\partial u} \phi_g(u,v,w) \right]_{u=0} dv\, dw$$

The right-hand surface partial currents, $J_{gur}^{in,m}$ and $J_{gur}^{out,m}$, fulfill

$$-J_{gur}^m = J_{gur}^{in,m} - J_{gur}^{out,m}$$

where the total current is defined as above with the replacement of u = 0 with $u = a_u^m$. The following sketch clarifies this notation:

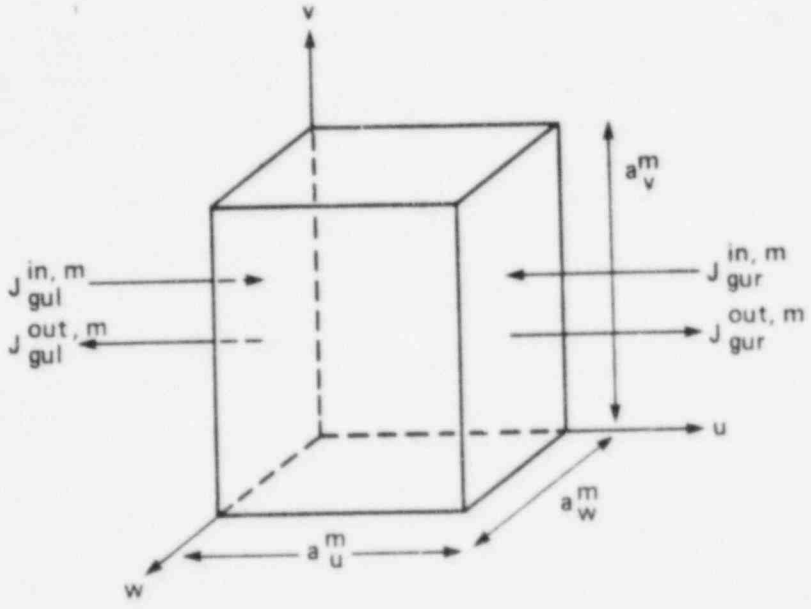

No approximations were made to obtain the nodal balance equation, equation (2-2). However, to obtain a closed set of equations, an expression must be obtained relating partial currents and the nodal flux. In NEM, this expression is found, as described in the following section, by integrating the diffusion equation in the two transverse directions. This integration results in a one-dimensional diffusion equation. Here, physical parameters, such as cross sections, are assumed to be constant across a node. As described in subsection 2-1-2, spatial variation across a node induced by burnup and feedback is allowed.

The one-dimensional diffusion equations are obtained by integrating the three-dimensional diffusion equation, equation (2-1), over a rectangular plane of area $a_v^m a_w^m$ normal to the direction of interest, u,

$$- \tilde{D}_g^m \frac{d^2 \psi_{gu}^m(u)}{du^2} + \tilde{\Sigma}_{tg}^m \psi_{gu}^m(u) - Q_{gu}^m(u) + L_{gu}^m(u) = 0 \qquad (2\text{-}3)$$

where the one-dimensional flux, source, and transverse leakage are written

$$\psi^m_{gu}(u) = \frac{1}{a^m_v \; a^m_w} \int_0^{a^m_v} \int_0^{a^m_w} \phi_g(u,v,w)\, dv\, dw$$

$$Q^m_{gu}(u) = \frac{1}{a^m_v \; a^m_w} \int_0^{a^m_v} \int_0^{a^m_w} \sum_{g'} \left(\Sigma_{g'g} + \frac{\chi_g}{\lambda} \nu\Sigma_{fg'}\right) \phi_{g'}(u,v,w)\, dv\, dw$$

$$= \sum_{g'} \left(\bar{\Sigma}_{g'g} + \frac{\chi_g}{\lambda} \nu\bar{\Sigma}_{fg'}\right) \frac{1}{a^m_v \; a^m_w} \int_0^{a^m_v} \int_0^{a^m_w} \phi_{g'}(u,v,w)\, du\, dw$$

$$= \sum_{g'} \left(\bar{\Sigma}_{g'g} + \frac{\chi_g}{\lambda} \nu\bar{\Sigma}_{fg'}\right) \psi^m_{g'u}(u)$$

$$L^m_{gu}(u) = \frac{1}{a^m_v \; a^m_w} \int_0^{a^m_v} \int_0^{a^m_w} \left(\frac{\partial J_{vg}}{\partial v} + \frac{\partial J_{wg}}{\partial w}\right) dv\, dw$$

$$= \frac{1}{a^m_v \; a^m_w} \int_0^{a^m_w} \left[J_{vg}(u, v = a^m_v, w) - J_{vg}(u, v = 0, w)\right] dw$$

$$+ \frac{1}{a^m_v \; a^m_w} \int_0^{a^m_v} \left[J_{wg}(u, v, w = a^m_w) - J_{wg}(u, v, w = 0)\right] dv$$

The one-dimensional flux is approximated by the polynomial expansion

[ ]a,c

where the dimensionless spatial variable is

$$u' = \frac{u}{a^m_u}$$

and the expansion polynomials are chosen as

[ ] a,c

The expansion coefficients are found by a variety of means. [

]a,c

[ ] a,c (2-4)

[ ] a,c (2-5) (2-6)

where

[ ] a,c

[ ] a,c

and

[ ] a,c

At this point, two terms, [ ], a,c must still be found:

[ ] a,c

(2-7)

However, an additional approximation must first be made; the transverse leakage is represented by a quadratic polynomial

[ ] a,c

(2-8)

where [ ] a,c

The unknown coefficients, [ ]a,c, can now be found by the weighted residual method:

[ ] a,c (2-9)

n = 1,2

Substitution of the polynomial expansion for $L^m_{gu}(u)$ yields two matrix equations that can be solved to find C^m_{3gu} and C^m_{4gu} in terms of lower order coefficients, transverse leakage coefficients, the multiplication constant, and nodal physical properties. The flux expansion is substituted into tne definition of Fick's Law at the left and right surfaces,

[ ] a,c (2-10)

Solving these equations simultaneously yields the coupling equations:

[ ] a,c (2-11a)

and

[ ] a,c (2-11b)

The coupling coefficients are simple functions of the node width and diffusion theory constants. Substituting equation (2-11) into the nodal balance equation, equation (2-2), gives an expression relating the nodal average flux to the three sets of one-dimensional coupling coefficients, the incoming interface currents, and higher order flux coefficients.

[ ] a,c (2-12)

2-1-2 Boundary Conditions

Three types of boundary conditions are allowed in ANC: albedo boundary, cyclic boundary, and diagonal symmetry boundary. The albedo boundary condition can be applied to the fuel-reflector interface or to the outer surface of the reflector. No upscattering is assumed, so the albedo condition has the following general form:

$$\begin{pmatrix} J_1^{in,m} \\ J_2^{in,m} \end{pmatrix} = \begin{pmatrix} \alpha_{11} & 0 \\ \alpha_{21} & \alpha_{22} \end{pmatrix} \begin{pmatrix} J_1^{out,m} \\ J_2^{out,m} \end{pmatrix} \qquad (2\text{-}13)$$

The zero current boundary condition is represented by $\alpha_{11} = \alpha_{22} = 1.0$ and $\alpha_{21} = 0.0$

2-1-3 Iteration Solution Procedure

Equations (2-11) and (2-12) are solved iteratively to find the converged interface current distribution by the following procedure:

(1) [

]a,c

(2) [

]a,c

$$\left[\quad\right]^{a,c} \tag{2-14a}$$

and

$$\left[\quad\right]^{a,c} \tag{2-14b}$$

(3) [

]a,c

(4) Go to Step (1) and repeat until convergence is achieved.

The eigenvalue is found through a conventional power iteration. The following features are incorporated to ensure that the procedure is efficient and stable:

- o [ ]a,c
- o [ ]a,c
- o [ ]a,c

2-1-4 Nodal Expansion Method With Feedback Correction

Two types of intranodal heterogeneities must be accounted for in nodal calculations. One is the structural heterogeneity, and the other is the burnup- and feedback-induced heterogeneity. The structural heterogeneity is accounted for by the equivalence procedure described in subsection 2-3. The burnup- and feedback-induced intranodal heterogeneity can be accounted for by a second homogenization. [

]a,c

[

a,c

(2-15)

and

[

a,c

(2-16)

where

Σ_g^m = volume-weighted cross section

$\tilde{\tilde{\Sigma}}_g$ = effective volume-flux weighted cross section

$\tilde{\Sigma}_g(u)$ = area-flux weighted cross section on vw plane at u

$\delta_g^m(u)$ = correction to the transverse leakage due to feedback-induced heterogeneity

In ANC, the nonlinear term, [ ]^{a,c}, is evaluated using the flux solution of the preceeding iteration:

[ ]^{a,c} (2-17)

[

]^{a,c}

2-2 ROD POWER RECOVERY

After the global solution is obtained, the intranodal rod power distribution is recovered for every node by using an efficient superposition procedure. From this rod power distribution, peak rod power and hot channel factors are obtained and edited for each assembly. The rod power distribution is a product of the average nodal power ($\tilde{P}_g$), a form factor [ ], ^{a,c} and a rod factor [ ]; ^{a,c}

[ ]^{a,c} (2-18)

where

$$p^{ANC}_{g,homo}(x,y) = \kappa\bar{\Sigma}_{fg}\ \phi^{ANC}_{g,homo}(x,y)$$

$$p^{spectrum}_{g,hete}(x,y) = \kappa\Sigma_{fg}(x,y)\ \phi^{spectrum}_{g,hete}(x,y)$$

and

$$p^{spectrum}_{g,homo}(x,y) = \kappa\bar{\Sigma}_{fg}\ \phi^{spectrum}_{g,homo}(x,y)$$

[

]^{a,c} The rest of this subsection details the construction of these analytical solutions.

2-2-1 General Solution to the Two-Group Two-Dimensional Diffusion Equation

The analytic solutions, [ ]^{a,c} are found by the group theory approach[5] which takes advantage of the nodal symmetry transformations to construct the fast and thermal flux distributions.

The two-group diffusion equation can be written in the following matrix form:

$$\begin{pmatrix} D_1\nabla^2 - \Sigma_{t1} & 0 \\ +\Sigma_R & D_2\nabla^2 - \Sigma_{a2} \end{pmatrix} \begin{pmatrix} \phi_1 \\ \phi_2 \end{pmatrix} = -\frac{1}{k_{eff}} \begin{pmatrix} \nu\Sigma_{f1} & \nu\Sigma_{f2} \\ 0 & 0 \end{pmatrix} \begin{pmatrix} \phi_1 \\ \phi_2 \end{pmatrix} \qquad (2\text{-}19)$$

The eigenvalues of the above equations are

$$\mu^2 = \frac{1}{2}\left[-\left(\frac{1}{L_1^2}+\frac{1}{L_2^2}\right)+\sqrt{\left(\frac{1}{L_1^2}+\frac{1}{L_2^2}\right)^2+\frac{4(\kappa-1)}{L_1^2 L_2^2}}\right]$$

$$-\nu^2 = \frac{1}{2}\left[-\left(\frac{1}{L_1^2}+\frac{1}{L_2^2}\right)-\sqrt{\left(\frac{1}{L_1^2}+\frac{1}{L_2^2}\right)^2+\frac{4(\kappa-1)}{L_1^2 L_2^2}}\right]$$

Where

$$\frac{1}{L_1^2} = \frac{\Sigma'_{t1}}{D_1}$$

$$\frac{1}{L_2^2} = \frac{\Sigma_{a2}}{D_2}$$

$$\kappa = \frac{\Sigma_R}{\Sigma'_{t1}\ \Sigma_{a2}}\ \frac{\nu\Sigma_{f2}}{k_{eff}}$$

and

$$\Sigma'_{t1} = \Sigma_{t1} - \frac{1}{k_{eff}}\ \nu\Sigma_{f1}$$

The diagonalized two-group diffusion operator has the following form:

$$\begin{pmatrix} \nabla^2+\mu^2 & 0 \\ 0 & \nabla^2-\nu^2 \end{pmatrix}\ \begin{pmatrix} \phi_\mu \\ \phi_\nu \end{pmatrix} = 0 \qquad (2\text{-}20)$$

where ϕ_μ represents the asymptotic mode solution and ϕ_ν represents the transient solution of the two-group diffusion equation. The asymptotic mode is the solution present away from the boundary. The transient mode has a decay length approximately equal to the thermal group diffusion length and exists only near the material boundary. The fast and thermal fluxes are obtained by combining the asymptotic and transient solutions:

$$\phi_1 = \phi_\mu + \phi_\nu$$
$$\phi_2 = \alpha\phi_\mu + \beta\phi_\nu \qquad (2\text{-}21)$$

where

ϕ_1 = fast flux

ϕ_2 = thermal flux

$\alpha = \Sigma_R/(\Sigma_{a2} + D_{2\mu}{}^2)$

$\beta = \Sigma_R/(\Sigma_{a2} - D_{2\nu}{}^2)$

To complete the specific solution of equation (2-19) in an arbitrary region, V, a boundary condition along the border, ∂V, must be specified. The nodal solution provides such a boundary condition for each node in terms of the average surface partial currents:

$$\bar{\phi}^m_{gsu} = 2\left(J^{out,m}_{gsu} + J^{in,m}_{gsu}\right) \qquad (2\text{-}22)$$

where

u = x, y direction

s = r: right surface
    l: left surface

J = Average incoming (or outgoing) surface currents

The solution to equation (2-20) is a linear combination of terms of the form

[ ]a,c

and

[ ]a,c

where

[ ]a,c

[ ]a,c (2-23)

[ ] a,c (2-24a)

and

[ ] a,c (2-24b)

2-2-2 Construction of an Irreducible Representation

[ ] a,c

[

a,c

(2-25)

(2-26)

(2-27)

(2-28)

]

[ ] a,c

(2-29)

The following diagram shows the symmetry of these integrals.

[ ] a,c

[

]a,c

2-2-3 Decomposition of the Boundary Conditions

The two-group surface fluxes (or currents) are first projected into the asymptotic and transient modes.

[ ]a,c (2-30)

where

u = x, y

and

s = { l - left
    { r - right

The asymptotic surface flux and the transient surface flux can be further decomposed into symmetry components. For simplicity, we consider only the average nodal surface flux

[a,c]

(2-31)

where $\bar{m}_{j,\omega}$ has the same symmetry properties as Γ_j and can be calculated as

[ ]a,c (2-32)

and

[ ]a,c

Because the symmetry components are orthogonal, the components of the analytical solution are uniquely determined from the corresponding component of the boundary condition. That is, given a continuous function $m_{j,\omega}(v)$, at the boundary, u_s,

[ ]a,c (2-33)

the weighting function, $w_{j\omega}(\theta)$, can be obtained by a [ ]a,c However, in ANC, only an approximate shape of the boundary flux is expressed in terms of a lower-order polynominal. [

]a,c Therefore, only one base vector, defined by $\theta^{(\mu)}$, is necessary:

[ ]a,c (2-34)

and

[ ]a,c (2-35)

[ ]a,c

For the transient flux, it was found that because of [ ]a,c and the following expression is chosen:

[ ]a,c (2-36)

[ ]a,c

[ ]a,c (2-37)

and

[ ] a,c (2-38)

where ε is an empirically determined small distance approximately equal to a rod pitch.

[

]a,c

[

]a,c

2-3 CROSS SECTION HOMOGENIZATION

In ANC, as in other nodal codes, each node is assumed to be homogeneous and is represented by a set of diffusion theory constants. In nodal methods, neutronic parameters are traditionally obtained by simple volume and flux weighting; that is:

$$\bar{\Sigma}_{\alpha g} = \frac{\int \Sigma_{\alpha g}(\underline{r})\, \phi_g(\underline{r})\, d\underline{r}}{\int \phi_g(\underline{r})\, d\underline{r}} \qquad (2\text{-}39)$$

This equation for volume-flux weighted diffusion theory constants guarantees that in the homogeneous global calculation if the average flux is predicted correctly, the reaction rate, and therefore the power distribution and reactivity, will be predicted correctly. However, there are no a priori reasons that the average flux found in the homogeneous calculation will be the same as that found in the heterogeneous case.

As an example, we examine the homogenization of the steel baffle and reflector. In figure 2-1, the solid curve is the thermal flux for a problem of two full assemblies and one reflector assembly, with the baffle reflector explicity represented. Using fluxes for the heterogeneous problem, the volume-flux weighted diffusion theory constants are computed for the baffle-reflector. The dotted curve is the flux solution using these homogeneous diffusion theory constants.

Figure 2-1 shows that both the total flux and core boundary current are incorrect. The direction of the neutron flow is wrong as well. In the discrete representation, neutrons are leaking out of the core into the steel baffle; in the homogeneous representation, current leaks into the core. This is not unexpected because the homogenization procedure, in effect, replaces the steel baffle with a mixture of steel and water. This figure shows the need to improve upon the volume-flux weighted cross section.

To ensure that the global calculations will reproduce the nodal average reaction rates, eigenvalues, and so forth, the nodal boundary currents of the homogeneous node should be forced to agree with the heterogeneous node. This can be achieved by introducing a flux discontinuity factor in the global calculation as proposed by Koebke[6] and detailed in the next paragraph.

Let us first examine the two-group one-dimensional diffusion equation

$$- \bar{D}_g \frac{d^2\psi_u(u)}{du^2} + \bar{\Sigma}_{tg}\, \psi_u(u) - Q_{gu}(u) + L_{gu}(u) = 0$$

where $Q_{gu}(u)$ is the neutron source in group g and $L_{gu}(u)$ is the transverse leakage. As mentioned before, the homogeneous solution will agree with the heterogeneous solution if the diffusion theory constants are obtained from equation (2-39) and the boundary current of the heterogeneous solution is imposed on the equation.

Given boundary currents, the solution to the differential equation is uniquely defined. The surface flux of the solution, ϕ_g^{homo}, generally does not agree with the heterogeneous flux. As shown in figure 2-2, to force the homogeneous current at the boundary to agree with the average currrent from the heterogeneous calculations, the thermal flux of the homogeneous solution at the core-reflector interface is about five times the heterogeneous result. Conversely, if the thermal flux of the homogeneous solution at the core-reflector boundary is increased by a factor of about five, then the core-reflector currents of the homogeneous and heterogeneous solutions, as well as the reaction rates, will agree.

The above-mentioned flux discontinuity has been implemented in the ANC code. [

]^{a,c} Equation (2-1) is then solved [ ]^{a,c} for the homogeneous flux [ ]^{a,c} A discontinuity factor is defined:

$$f_g = \frac{\phi_g^{hete}}{\phi_g^{homo}} \qquad (2\text{-}40)$$

This discontinuity factor is input to ANC [ ]^{a,c}

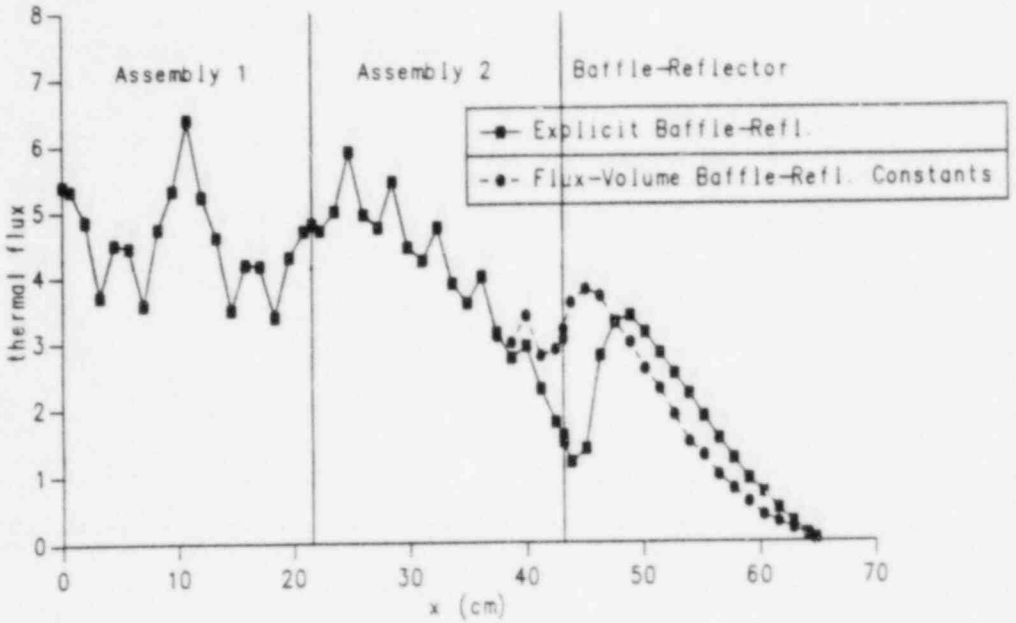

Figure 2-1. Baffle-Reflector Minicore Thermal Flux
Flux-Volume Weighted Constants

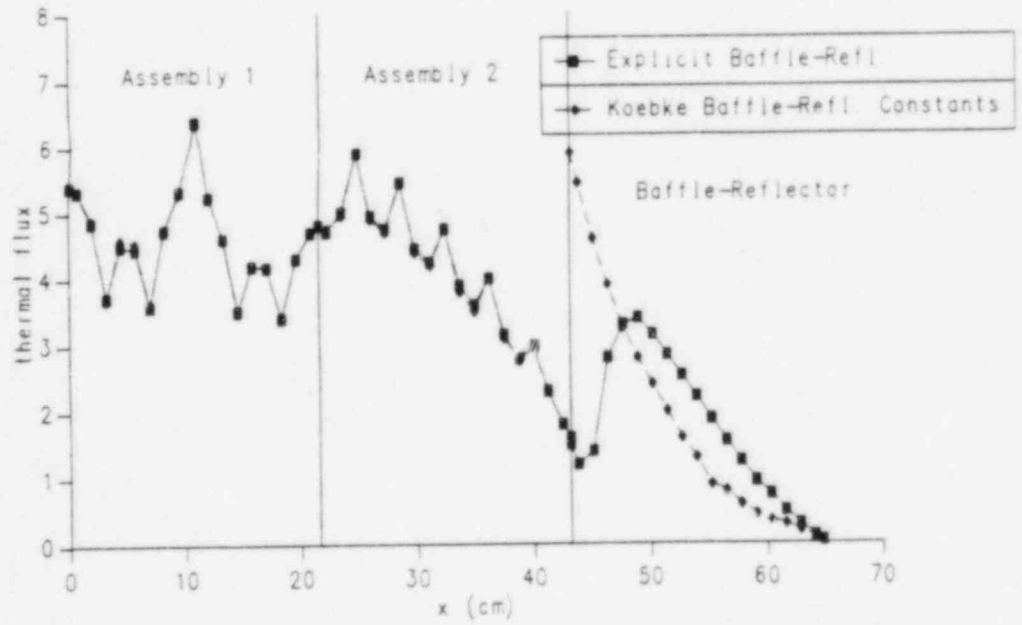

Figure 2-2. Baffle-Reflector Minicore Thermal Flux
Koebke Homogenized Constants

SECTION 3
ANC QUALIFICATION

Verifying and improving the PALADON code is an ongoing effort at Westinghouse, and this effort results in continuous improvement in the quality of the PALADON prediction. References 1 and 2 provide many benchmark comparisons of PALADON calculations with calculations performed with the Westinghouse discrete, fine-mesh, finite-difference, two-group diffusion theory design code and with plant measurements. This two-group diffusion theory code, TORTISE, is an updated version of the earlier TURTLE code.[7]

This section documents a similar set of benchmark comparisons of TORTISE calculations and measurements with calculations made using the ANC methodology which has been incorporated into PALADON. These comparisons severely test the ability of each component of the ANC methodology -- namely, the polynomial expansion representation of the one-dimensional flux and transverse leakage, the group theory rod power recovery procedure, and the equivalence theory of homogenization.

The polynomial expansion representation is tested by comparing measured data and predictions of fine-mesh diffusion codes for axial and radial power with ANC predictions. The comparison of TORTISE and ANC predicted rod powers given in subsection 3-1-3 provides a measure of the accuracy of the rod power recovery procedure in ANC and, it follows, that of the thimble flux prediction. The magnitude of radial power tilts or of any biases in rodded or burnable absorber assembly power predictions and the accuracy of predictions of critical boron concentrations are reported in this section to demonstrate the adequacy of the homogenization technique.

In all ANC calculations reported here, the baffle-reflector is [

].[a,c]

The data base for normal and off-normal conditions comprises three Westinghouse plants for a total of five cycles and includes first cores and reload cores. These plants are designated plant A, cycle 8; plant B, cycle 1; and plant C, cycles 1, 2, and 3. Data from this data base are presented in figures and tables which are grouped at the end of this section according to the number and title of the subsection in which they are discussed.

3-1 CORE DESIGN APPLICATION: NORMAL CONDITIONS

In this subsection, ANC predictions for normal operation conditions are compared with measurements and TORTISE predictions. Included in this subsection are comparisons of eigenvalues and critical boron concentrations, assembly average power distributions, axial power profiles, and reactivity coefficients.

3-1-1 Eigenvalue and Critical Boron Concentration

Comparison of eigenvalues and critical boron concentrations calculated by ANC and TORTISE verifies the capability of ANC to predict reactivity. Although the IAEA benchmark problem[8] shown in figure 3-1 is not part of the data base mentioned previously, it provides an opportunity to test the ANC eigenvalue predictive capability alone. This problem, which is used internationally to benchmark nodal codes, consists of three homogeneous regions and homogeneous control rod zones. Because the cross sections of these regions are completely specified by the problem, homogenization procedures are not an issue. Calculated differences, therefore, are due only to approximations of the method. The K_{eff} predicted by ANC is [ ]^{b,c} which, when compared to the benchmark value of 1.02959, differs by only [ ]^{b,c} pcm. The power distributions agree well, as shown in figure 3-2.

For actual heterogeneous cores, an additional homogenization step is required in ANC to produce nodal cross sections from discrete rod cell and fuel assembly structure cross sections. (This step is not required in TORTISE.) If performed incorrectly, this homogenization step will introduce a deviation between ANC and TORTISE predictions of critical boron concentration calculated as a function of core life for plants in the data base.

No significant deviations were found (table 3-1). For [ ]^{b,c} data points, the critical boron concentration predictions of ANC and TORTISE differ by only [ ]^{b,c} ppm, on the average. The standard deviation of [ ]^{b,c} ppm indicates the small variability of the data. A similar comparison of critical boron concentrations calculated by PALADON and TORTISE for a different data base yielded a mean difference of [ ]^{b,c} ppm and a standard deviation of [ ]^{b,c} ppm.[2] Figures 3-3 through 3-7 and tables 3-2 through 3-6 illustrate the excellent agreement between ANC and TORTISE for all the cores in the data base throughout cycle life.

The excellent critical boron concentration prediction of ANC (compared with TORTISE) demonstrates the accuracy of the eigenvalue predictive capability of ANC. The nearly undetectable deviation of the calculated eigenvalue for the IAEA problem further supports this conclusion.

3-1-2 Assembly Average Power Distribution

Assembly average power distribution comparisons were made between ANC and TORTISE at the burnups and boron concentrations tabulated in subsection 3-1-1 for the five cycles. A statistical summary of the comparisons is presented in table 3-7. Beginning-of-life, end-of-life, and cumulative total cycle data have been averaged over the five cycles. In addition, to identify any possible bias in the prediction of assembly power caused by the location of assemblies in the core or by the presence of burnable absorbers (BP), analysis of five subsets of the entire data base is presented. The five subsets of the data base are (1) assemblies that neither contain burnable absorber nor are located on the periphery of the core, (2) assemblies without burnable absorbers, (3) assemblies containing burnable absorbers, (4) assemblies located on the core periphery, and for completeness, (5) assemblies located away from the core periphery.

Over the entire data base comprising [ ]^{b,c} assemblies, a mean difference of only [ ]^{b,c} percent from ANC data to TORTISE data is revealed, with a standard deviation of [ ]^{b,c} percent. This small difference indicates that no systematic bias exists between the two methods. No significant bias is seen in any subcategory. The peripheral assembly comparison shows the

largest mean difference ([ ]^{b,c} percent) and the largest standard deviation ([ ]^{b,c} percent). In general, peripheral assemblies operate at significantly lower power levels than do other assemblies in the core. This slight mean difference is attributed to [

]^{a,c}

Comparisons of TORTISE and ANC assembly average power distributions are presented for the three cycles of plant C at beginning and end of life in figures 3-8 through 3-13.

The IAEA benchmark problem was also used for power distribution comparison. The comparison of assembly power predicted by ANC and the reference solution is shown in figure 3-2. These results indicate good agreement with maximum deviations of [ ]^{b,c} percent.

The good agreement between ANC assembly average powers and TORTISE-predicted values demonstrates the accuracy of core power distribution prediction of ANC. The excellent predictions established for the IAEA benchmark problem and the results discussed in subsection 3-1-1 verify the adequacy of the Nodal Expansion Methodology and the cross section homogenization precedure used in the ANC methodology.

3-1-3 Rod Power Comparison

As explained in subsection 2-2, after making the global nodal calculation, ANC recovers the rod-by-rod power distribution by superposing form factors on the assembly average power. These form factors are constructed from the surface fluxes obtained during the global calculation and from precalculated rod factors. The rod with the maximum power in each assembly is determined from the assembly rod power distribution. Its power is known as the assembly peak power. The adequacy of this approach is demonstrated in this subsection by comparing the ANC and TORTISE assembly peak powers and detailed rod-by-rod power distributions of selected assemblies.

Table 3-8 is a statistical comparison of the ANC and TORTISE assembly peak powers. For a data base of [ ]^{b,c} assemblies, the mean difference in

assembly peak rod power is [ ]^{b,c} percent, and the standard deviation is [ ]^{b,c} percent, compared with the corresponding PALADON values of [ ]^{b,c} percent and [ ]^{b,c} percent. For the peripheral assemblies, the mean difference and the standard deviation are [ ]^{b,c} percent and [ ]^{b,c} percent, compared to the corresponding PALADON values of [ ]^{b,c} percent and [ ]^{b,c} percent. The average and spread of these data are greater than that of the assembly average power data, which indicates the greater difficulty of predicting rod power. For both average and peak powers, ANC compares more favorably with TORTISE than does PALADON. Comparisons of TORTISE and ANC assembly peak power distribution are presented for the three cycles of plant C at beginning and end of life in figures 3-14 through 3-19.

Table 3-9 summarizes the deviation between ANC and TORTISE in the prediction of the power in the rod that has the greatest power of all the rods in the core -- the core peak rod power. For the [ ]^{b,c} data points, which represent the total number of burnup steps analyzed for the five cores, the mean relative difference between ANC and TORTISE is only [ ]^{b,c} percent. The spread in these data is also very small, as indicated by the standard deviation of just [ ]^{b,c} percent.

The rod-by-rod power distribution comparisons of ANC and TORTISE given in figures 3-20 and 3-21 for two assemblies of plant C, cycle 3, further illustrate the level of accuracy of the ANC rod power recovery. The assemblies are located near the core periphery at location (6,6) and adjacent to the baffle at location (8,2). In general, as seen in assembly (6,6), the largest deviation occurs at [ ].^{b,c} In this case, these errors never exceed [ ]^{b,c} percent, and therefore no attempt was made to reduce them.

At [ ]^{b,c} of the assembly, the disagreement between TORTISE and ANC rod powers is [ ].^{b,c} Assembly (8,2), which is the location of the core peak rod power, exhibits a different power distribution. Because this assembly is located on the periphery, a large flux gradient is present because the flux decreases near the baffle. This gradient provides a severe test of the rod power recovery procedure. As evidenced by the small deviation

everywhere but the outermost edge of the assembly, the ANC rod powers are in excellent agreement with the TORTISE values. At the edge, where rod powers are relatively low (about 0.6), larger differences are observed.

An additional verification of the ability of ANC to predict rod power distribution is presented in figure 3-22. Shown is the measured integral reaction rates in instrumented thimbles of plant C, cycle 2, at a burnup of 11,000 MWD/MTU. Also presented are the percent differences from measurements of TORTISE and ANC predictions. These results indicate that ANC predictions are of comparable accuracy to TORTISE reaction rate predictions. ANC can be used to generate constants for INCORE,[9] as this good agreement and the consistent predictions of rod power show.

3-1-4 Axial Power Distribution

To verify the ability of ANC to predict three-dimensional power distributions, measured and ANC predicted core average axial power profiles are compared. Excellent agreement is shown in axial power shapes for the unrodded condition at various values of burnup (figures 3-23 through 3-27) and for a rodded configuration at beginning of life, hot zero power, with D-bank almost completely inserted (figure 3-28).

The measured and calculated values of axial offset are presented in table 3-10 for quantitative assessment of the agreement between measured and ANC predicted data. For the rodded case, the measured axial offset is [ ]^{b,c} percent; ANC calculates a value of [ ]^{b,c} percent.

3-1-5 Reactivity Coefficients

The ability of ANC to predict reactivity is discussed in subsection 3-1-1. ANC should predict reactivity coefficients to the same level of accuracy as it predicted reactivity itself.

Table 3-11 compares moderator temperature coefficients calculated by ANC and TORTISE. For a data base of [ ]^{b,c} unrodded cases, the mean difference is [ ]^{b,c} pcm/°F, with a standard deviation of [ ]^{b,c} pcm/°F. For [ ]^{b,c} cases with D-bank inserted, the corresponding values are

[ ]^{b,c} pcm/°F and [ ]^{b,c} pcm/°F. Table 3-12 displays excellent agreement in boron coefficients predicted by ANC and TORTISE, within [ ]^{b,c} percent for all [ ]^{b,c} cases studied.

3-1-6 Control Rod Worths

The ability of ANC to predict control rod worths is demonstrated by the data presented in table 3-13 and summarized in table 3-14. For a data base of [ ]^{b,c} cases, the mean difference between ANC and TORTISE rod worths is [ ]^{b,c} percent with a standard deviation of [ ]^{b,c} percent. The data base comprises results for four cycles and different rod patterns for beginning and end of life, and hot full and hot zero power.

3-2 CORE DESIGN APPLICATION: OFF-NORMAL CONDITIONS

ANC is intended to be used for all nuclear design calculations including off-normal condition analyses. These analyses include, but are not limited to, control rod worths and power distributions for ejected rod, stuck rod, and dropped rod. This subsection presents comparisons of ANC and TORTISE predictions to qualify the application of ANC to off-normal analyses.

3-2-1 Rod Ejection

Rod ejection calculations represent one of the most severe tests of a nodal code's ability because of the presence of extreme power peaking. Even under these severe conditions, it is evident from table 3-15 that ANC predicts accurate ejected rod worths and power distributions.

For the four cases studied, the largest error is [ ]^{b,c} percent in the maximum assembly power, [ ]^{b,c} percent in the maximum assembly peak power, and [ ]^{b,c} percent in the ejected rod worth. On the average, the maximum assembly peak power is predicted to within [ ]^{b,c} percent with a standard deviation of [ ]^{b,c} percent.

Figures 3-29 through 3-32 present assembly average powers of the four cycles analyzed. Assembly peak powers for plant C, cycle 2, are presented in figure 3-33. As shown in these figures, the difference between ANC and

TORTISE is, in general, greater than those seen in the normal operation comparisons presented earlier.

3-2-2 Stuck Rod

In both the stuck rod analysis and the ejected rod analysis, the power of the hottest rod in the core is found when the control rod with the greatest worth is stuck (or ejected) out of the core. The two analyses differ in the configuration of the remaining rods: for the stuck rod case, all control rods and shutdown rods are fully inserted; for rod ejection, the shutdown rods are fully withdrawn and the control rods are at the insertion limits. Usually, some shutdown rods are located in peripheral assemblies, which makes it difficult, even for fine-mesh diffusion codes, to simulate the stuck rod condition.

The assembly average power comparison presented in figures 3-34 through 3-36 and the peak powers of plant C, cycle 2, compared in figure 3-37, show close agreement between ANC and TORTISE predictions for the stuck rod condition, [ ].[b,c]

Table 3-16 summarizes the calculated stuck rod worths and the maximum assembly average and peak powers. The core peak power predicted by ANC deviates from that predicted by TORTISE by only [ ][b,c] percent with a standard deviation of [ ][b,c] percent.

3-2-3 Dropped Rod

The dropped rod analysis is a calculation performed at the most limiting condition (typically beginning of life, hot full power) with the rod of the greatest worth fully inserted in the core. As in the previous two analyses, the parameters of interest are the peak rod power and the worth of the dropped rod itself. Table 3-17, which summarizes the dropped rod worth and maximum assembly average and peak powers, demonstrates the excellent agreement between ANC and TORTISE predictions for the dropped rod analyses of four cores. On the average, the maximum assembly powers are predicted to within [ ][b,c] percent, although the peak power data shows slightly more spread than the average, as evidenced by the respective standard deviations of [ ][b,c] percent and [ ][b,c] percent.

Unlike the ejected rod and stuck rod conditions, where a large amount of positive reactivity is introduced, the dropped rod analysis is one of negative reactivity insertion, and therefore, the power distribution is skewed away from the rod position, rather than toward it, as it is in the other two cases. This is demonstrated in the full core assembly average power maps presented for four cores in figures 3-38 through 3-41 and in the assembly peak power comparison of figure 3-42.

The results discussed in subsection 3-2 indicate the ability of ANC to accurately predict reactivity and power distribution in the presence of strong power gradients, as typical of stuck, ejected, or dropped control rod configurations.

Figures and Tables for Subsection 3-1-1
Eigenvalue and Critical Boron Concentration

155838.1

Region	D_1	D_2	Σ_R	Σ_{a1}	Σ_{a2}	$\nu\Sigma_{f2}$
1	1.5	0.4	0.02	0.01	0.08	0.135
2	1.5	0.4	0.02	0.01	0.085	0.135
3	1.5	0.4	0.02	0.01	0.13	0.135
4	2.0	0.3	0.04	0	0.01	0

$\nu\Sigma_{f1}$ = 0 all regions

$B_z^2 = 0.8 \times 10^{-4}$

External boundaries $J_g^{in} = 0$

Symmetry boundaries $J_g = 0$

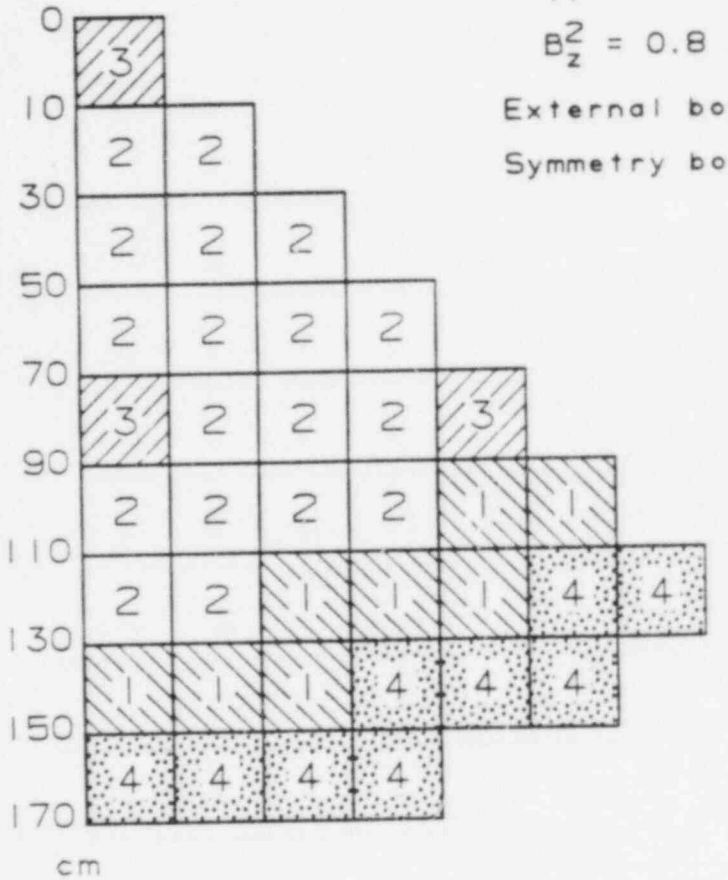

Figure 3-1. Two-Dimensional IAEA Benchmark Problem

Key: Reference
ANC
$\frac{(ANC - Reference)}{Reference} * 100$
(ANC - Reference)

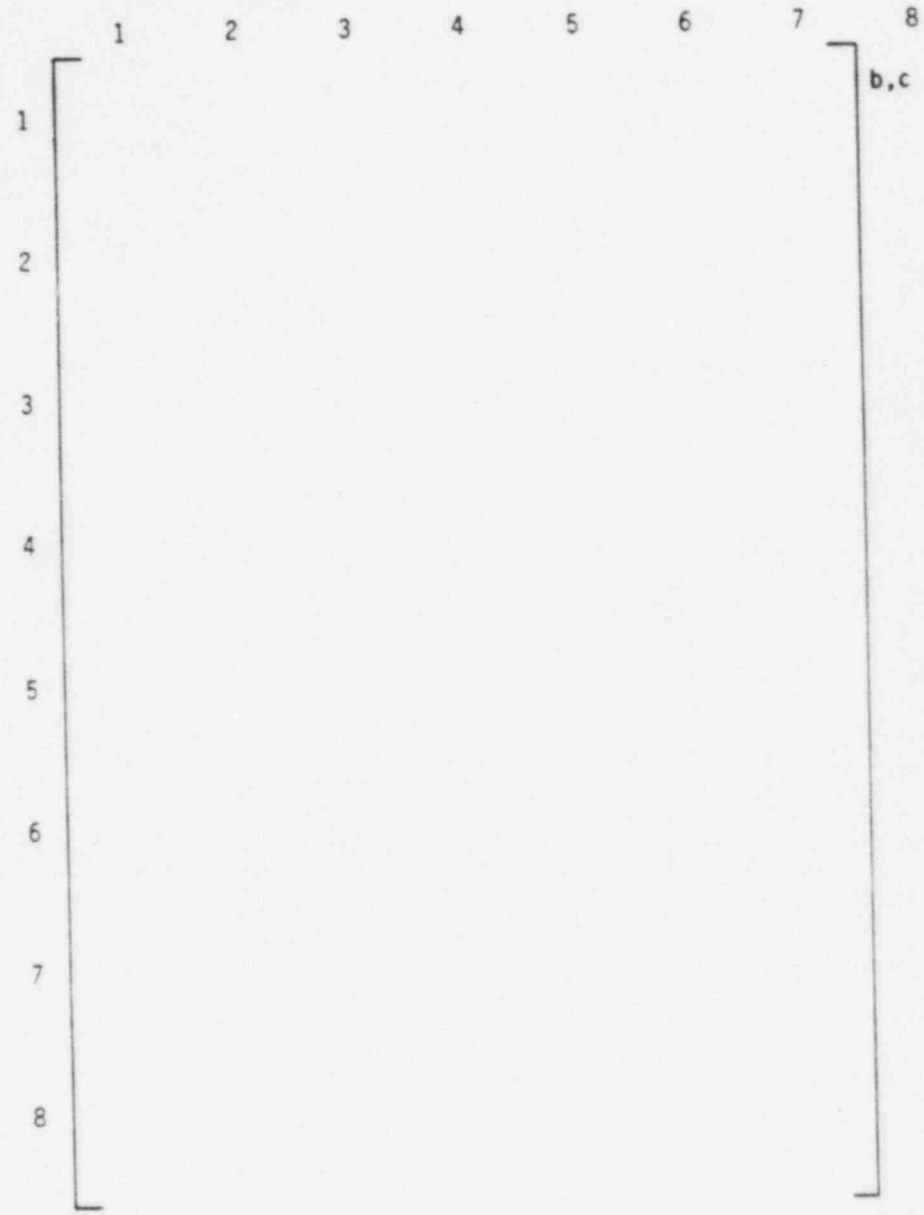

Figure 3-2. Two-Dimensional IAEA Benchmark Problem
ANC/Reference Solution
Assembly Average Power Comparison

TABLE 3-1
ANC AND TORTISE CRITICAL BORON COMPARISON SUMMARY

Plant/Cycle	Mean Difference* (ppm)	Standard Deviation (ppm)	N
Plant A, Cycle 8	[		] b,c
Plant B, Cycle 1			
Plant C, Cycle 1			
Plant C, Cycle 2			
Plant C, Cycle 3			
total database			

* ANC - TORTISE

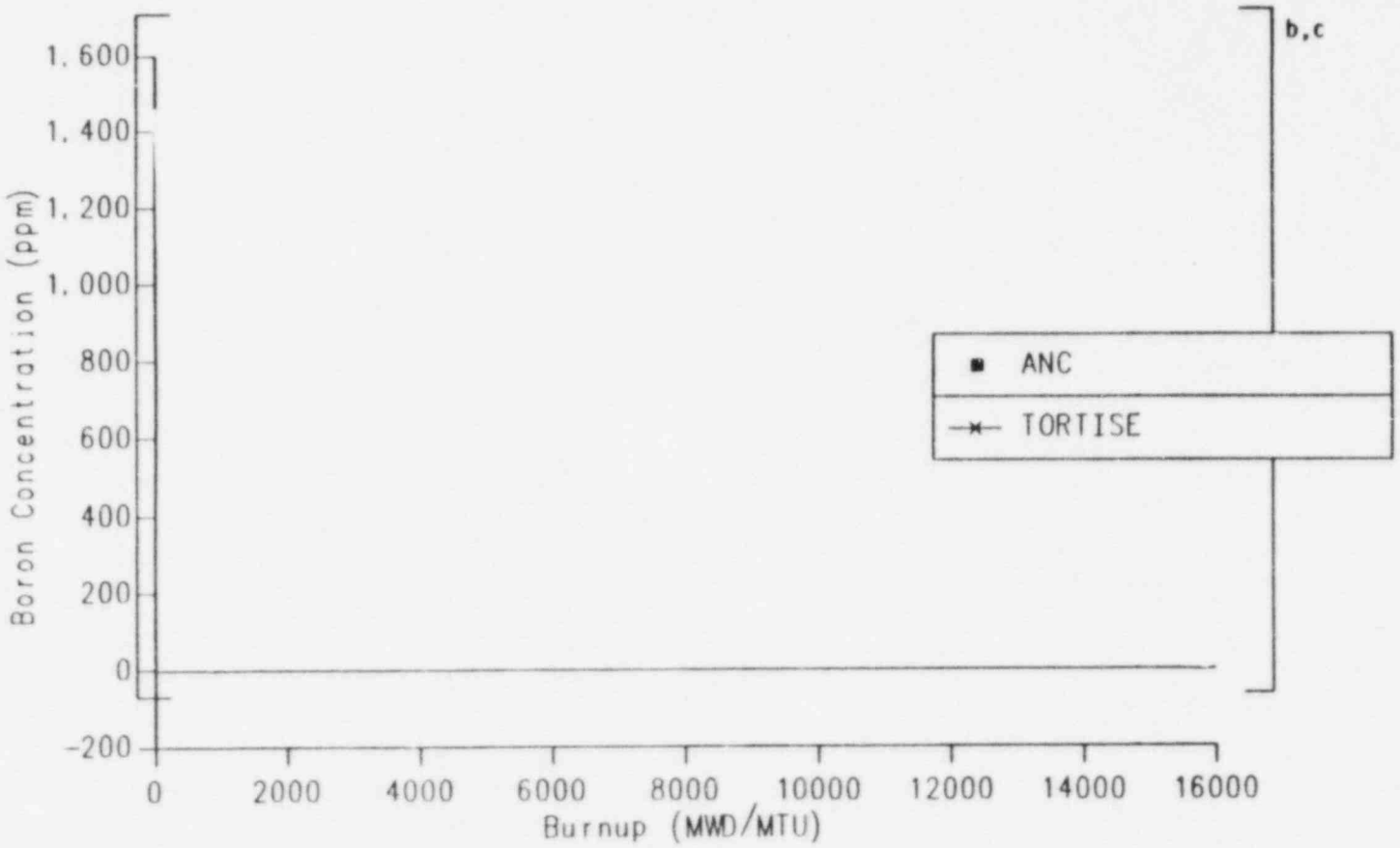

Figure 3-3. Boron Letdown Curve, ANC/TORTISE
Plant A, Cycle 8

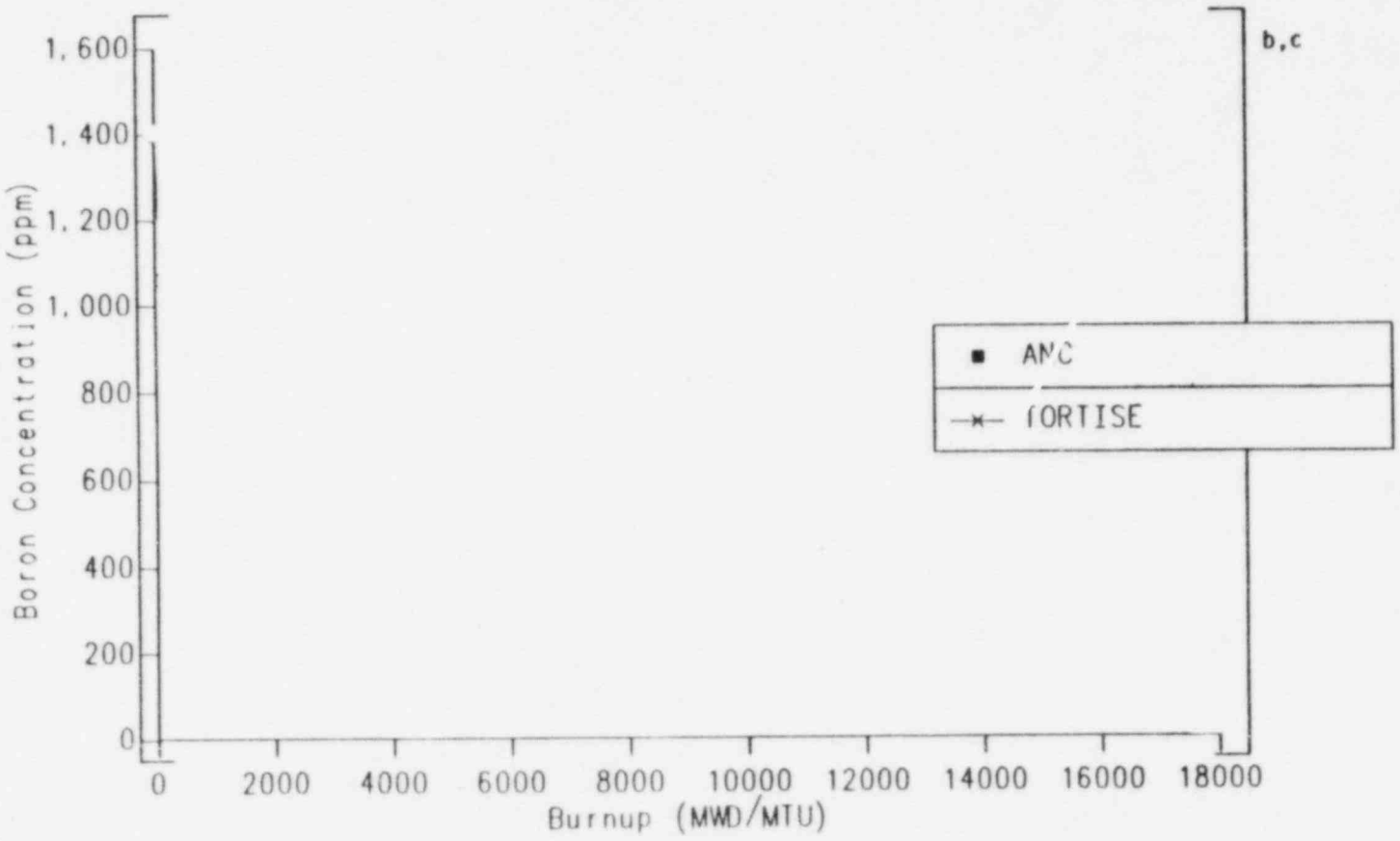

Figure 3-4. Boron Letdown Curve, ANC/TORTISE
Plant B, Cycle 1

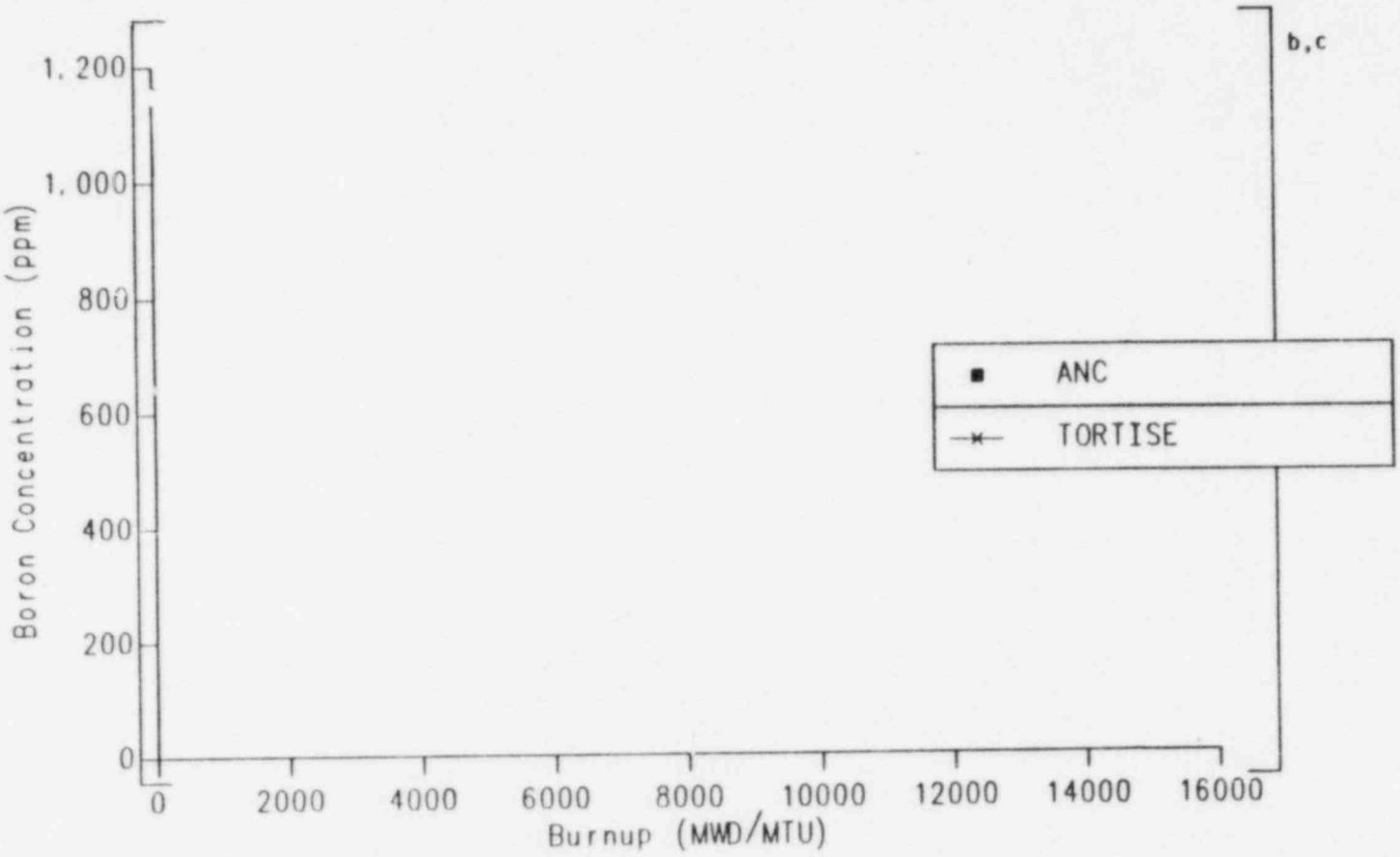

Figure 3-5. Boron Letdown Curve, ANC/TORTISE
Plant C, Cycle 1

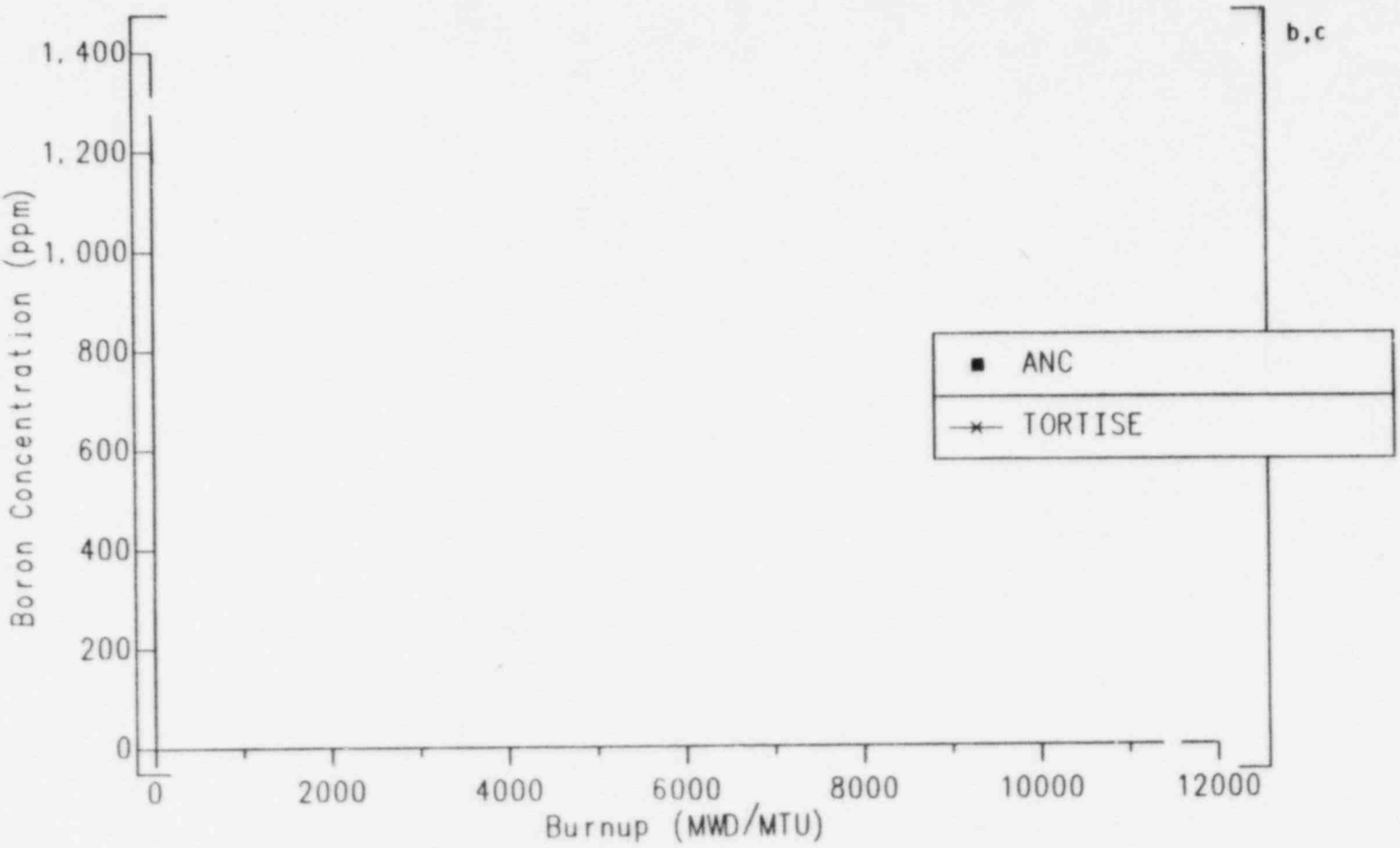

Figure 3-6. Boron Letdown Curve, ANC/TORTISE
Plant C, Cycle 2

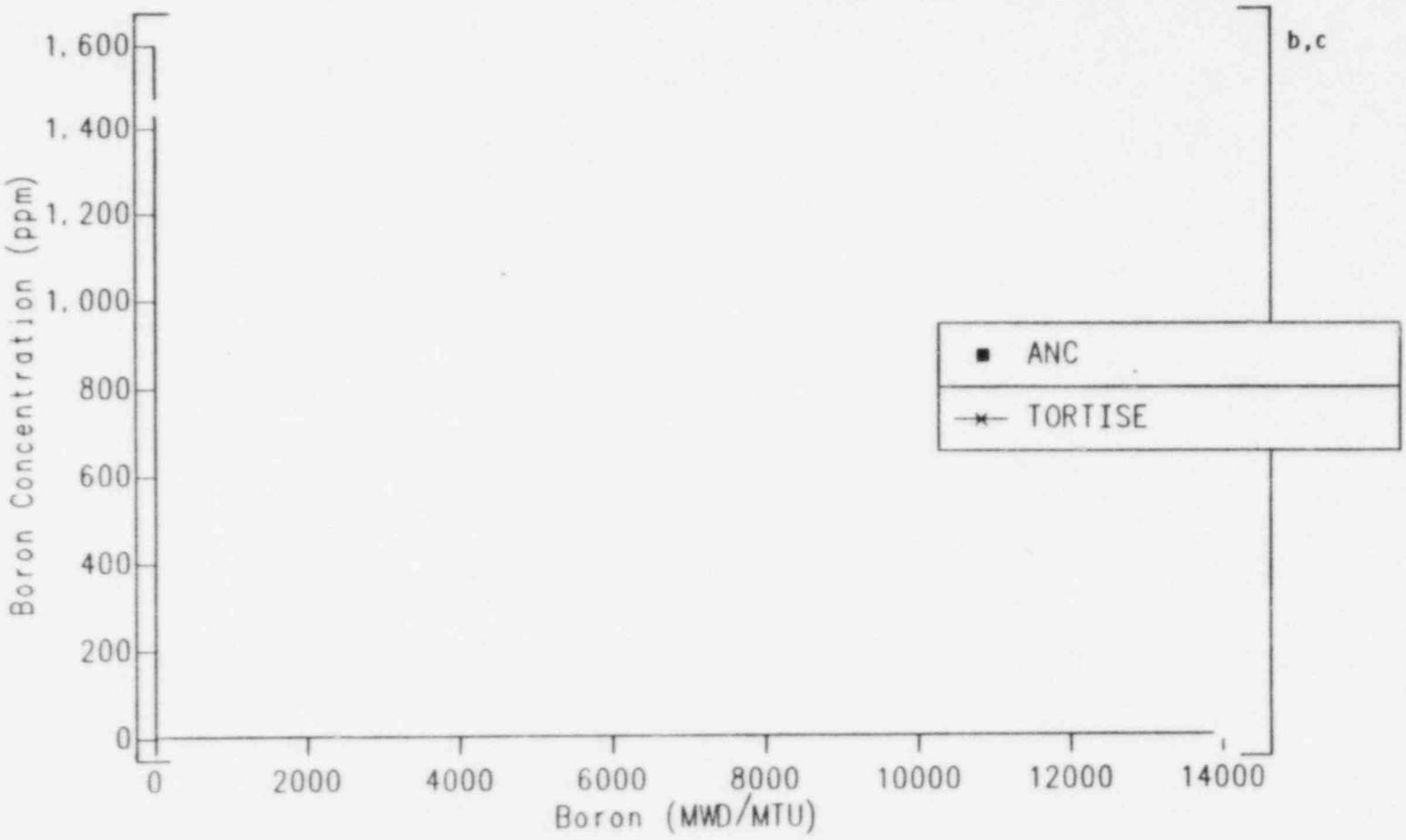

Figure 3-7. Boron Letdown Curve, ANC/TORTISE
Plant C, Cycle 3

TABLE 3-2
ANC AND TORTISE CRITICAL BORON COMPARISONS
NORMAL OPERATION, PLANT A, CYCLE 8

Step	Burnup (MWD/MTU)	Boron Concentration (ppm)		
		TORTISE	ANC	ANC - TORTISE
1	0	[		] b,c
2	150			
3	1000			
4	2000			
5	4000			
6	6000			
7	8000			
8	10000			
9	12000			
10	14000			
11	14950			
12	15750	]		
Mean Difference (ppm)		[	] b,c	
Standard Deviation (ppm)				

TABLE 3-3
ANC AND TORTISE CRITICAL BORON COMPARISONS
NORMAL OPERATION, PLANT B, CYCLE 1

Step	Burnup (MWD/MTU)	Boron Concentration (ppm)			
		TORTISE	ANC	TORTISE - ANC	
1	0	[			] b,c
2	150				
3	500				
4	1000				
5	2000				
6	3000				
7	4000				
8	5000				
9	6000				
10	8000				
11	10000				
12	12000				
13	14000				
14	16000				
15	17750				]

Mean Difference (ppm) [ ] b,c
Standard Deviation (ppm) [ ]

TABLE 3-4
ANC AND TORTISE CRITICAL BORON COMPARISONS
NORMAL OPERATION, PLANT C, CYCLE 1

Step	Burnup (MWD/MTU)	Boron Concentration (ppm)		
		TORTISE	ANC	ANC - TORTISE
1	0	[		] b,c
2	150			
3	500			
4	1000			
5	2000			
6	3000			
7	4000			
8	5000			
9	6000			
10	8000			
11	10000			
12	12000			
13	14000			
14	14750			

Mean Difference (ppm)	[ ] b,c
Standard Deviation (ppm)	

TABLE 3-5
ANC AND TORTISE CRITICAL BORON COMPARISONS
NORMAL OPERATION, PLANT C, CYCLE 2

Step	Burnup (MWD/MTU)	Boron Concentration (ppm)		
		TORTISE	ANC	ANC - TORTISE
1	0	[		] b,c
2	150			
3	500			
4	1000			
5	2000			
6	4000			
7	6000			
8	8000			
9	10000			
10	11500			
Mean Difference (ppm)		[		] b,c
Standard Deviation (ppm)		[		]

TABLE 3-6
ANC AND TORTISE CRITICAL BORON COMPARISONS
NORMAL OPERATION, PLANT C, CYCLE 3

Step	Burnup (MWD/MTU)	Boron Concentration (ppm)		
		TORTISE	ANC	ANC - TORTISE
1	0	[		] b,c
2	150			
3	1000			
4	2000			
5	4000			
6	6000			
7	8000			
8	10000			
9	12000			
10	14000			
Mean Difference (ppm)		[	] b,c	
Standard Deviation (ppm)		[	]	

Figures and Tables for Subsection 3-1-2
Assembly Average Power Distribution

TABLE 3-7
PERCENT DIFFERENCE IN ASSEMBLY AVERAGE POWER AS CALCULATED BY ANC AND TORTISE FOR NORMAL OPERATION

	Mean Difference* (%)	Standard Deviation (%)	N
Total Data Base			
BOL	[		] b,c
EOL			
entire cycle			
Non-BP and Non-Peripheral Assemblies			
BOL	[		] b,c
EOL			
entire cycle			
Non-BP Assemblies			
BOL			
EOL			
entire cycle			
BP Assemblies			
BOL			
EOL			
entire cycle			
Peripheral Assemblies			
BOL			
EOL			
entire cycle	]		]
Non-Peripheral Assemblies			
BOL	[		] b,c
EOL			
entire cycle	]		]

$$* \frac{(ANC - TORTISE)}{TORTISE} * 100\ \%$$

Key: TORTISE
ANC
(ANC - TORTISE) * 100
TORTISE
(ANC - TORTISE)

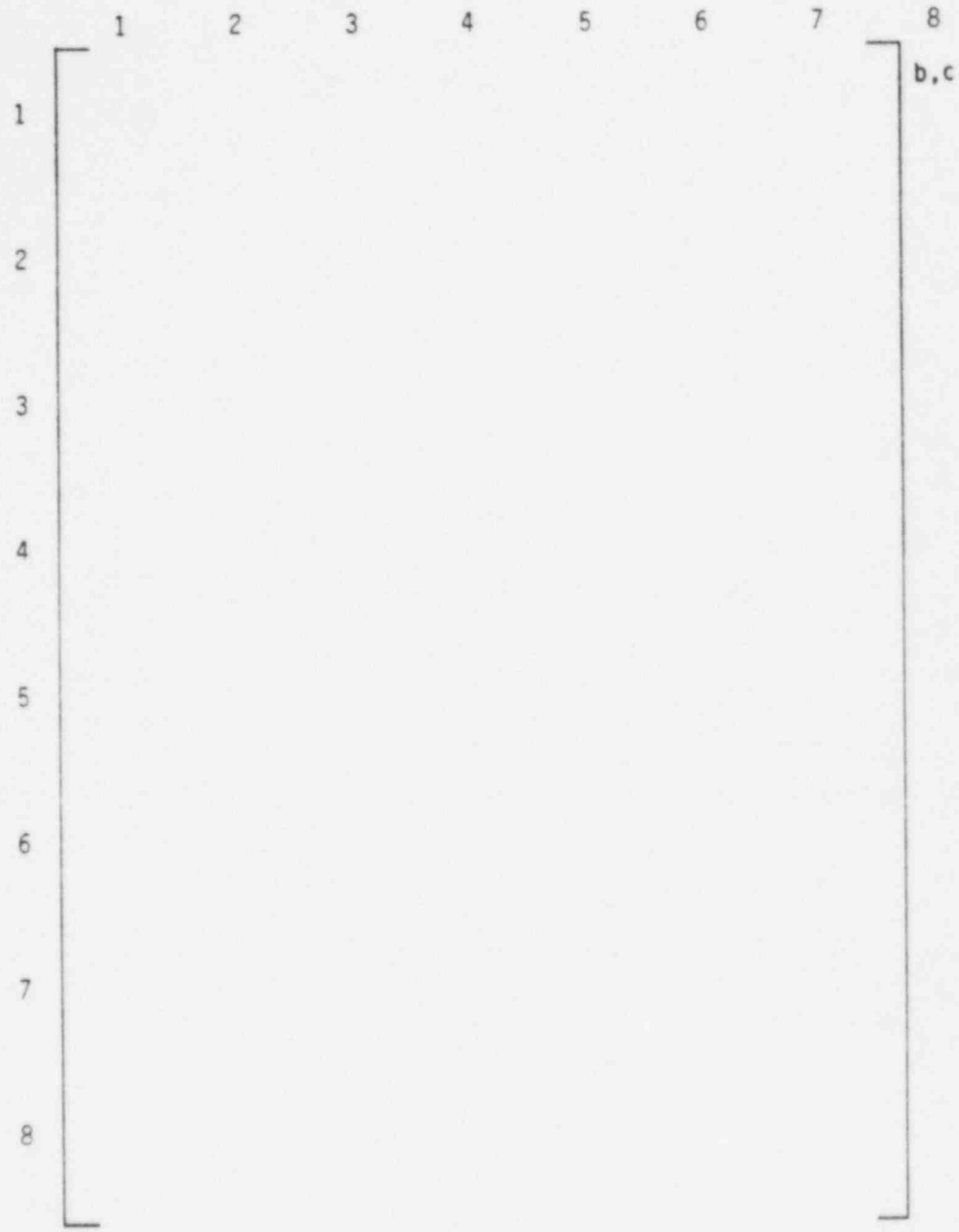

Figure 3-8. Assembly Average Power Comparison
Plant C, Cycle 1, BOL
Normal Operation, ANC/TORTISE

Key: TORTISE
ANC
(ANC - TORTISE) / TORTISE * 100
(ANC - TORTISE)

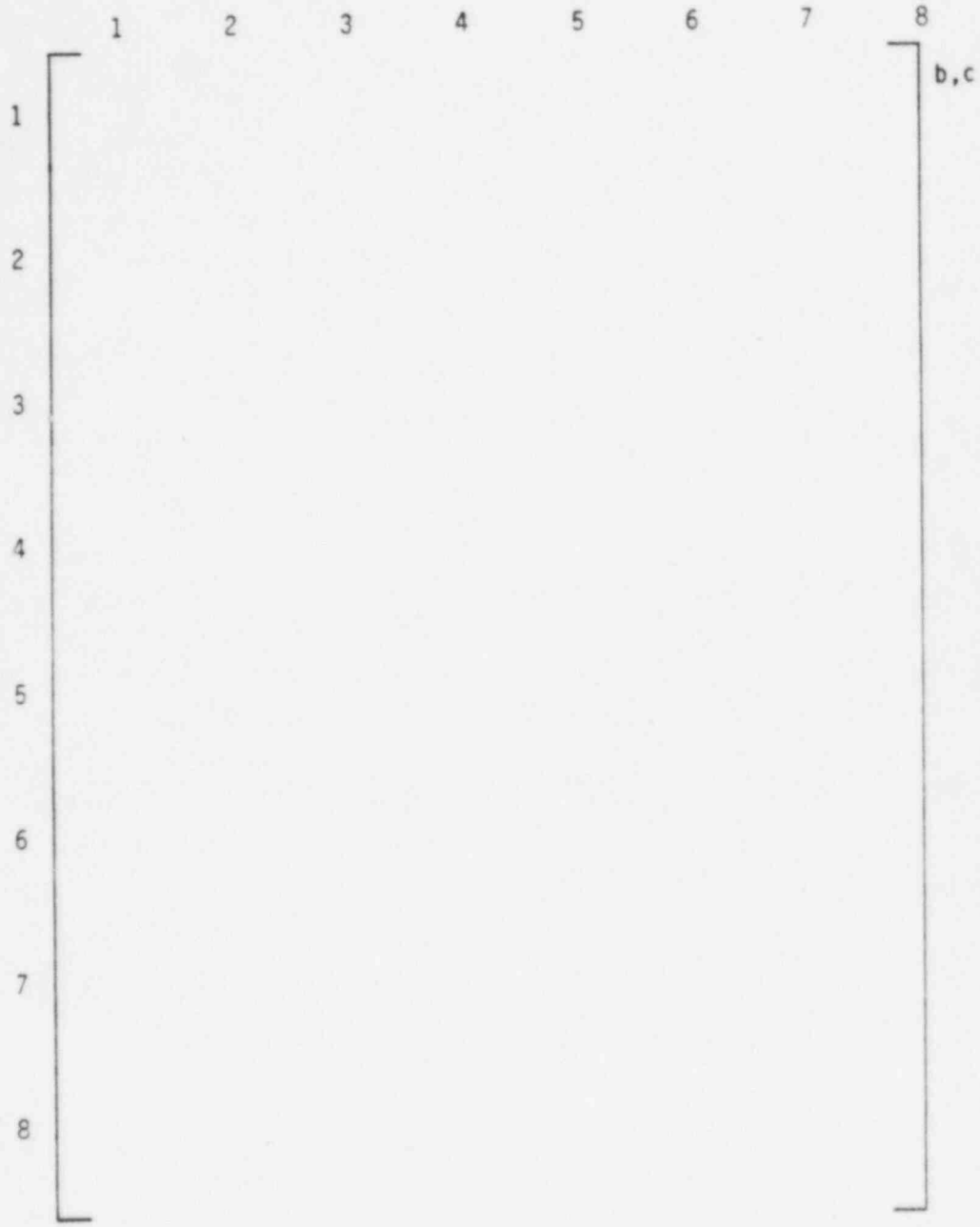

Figure 3-9. Assembly Average Power Comparison
Plant C, Cycle 1, EOL
Normal Operation, ANC/TORTISE

Key: TORTISE
ANC
(ANC - TORTISE) / TORTISE * 100
(ANC - TORTISE)

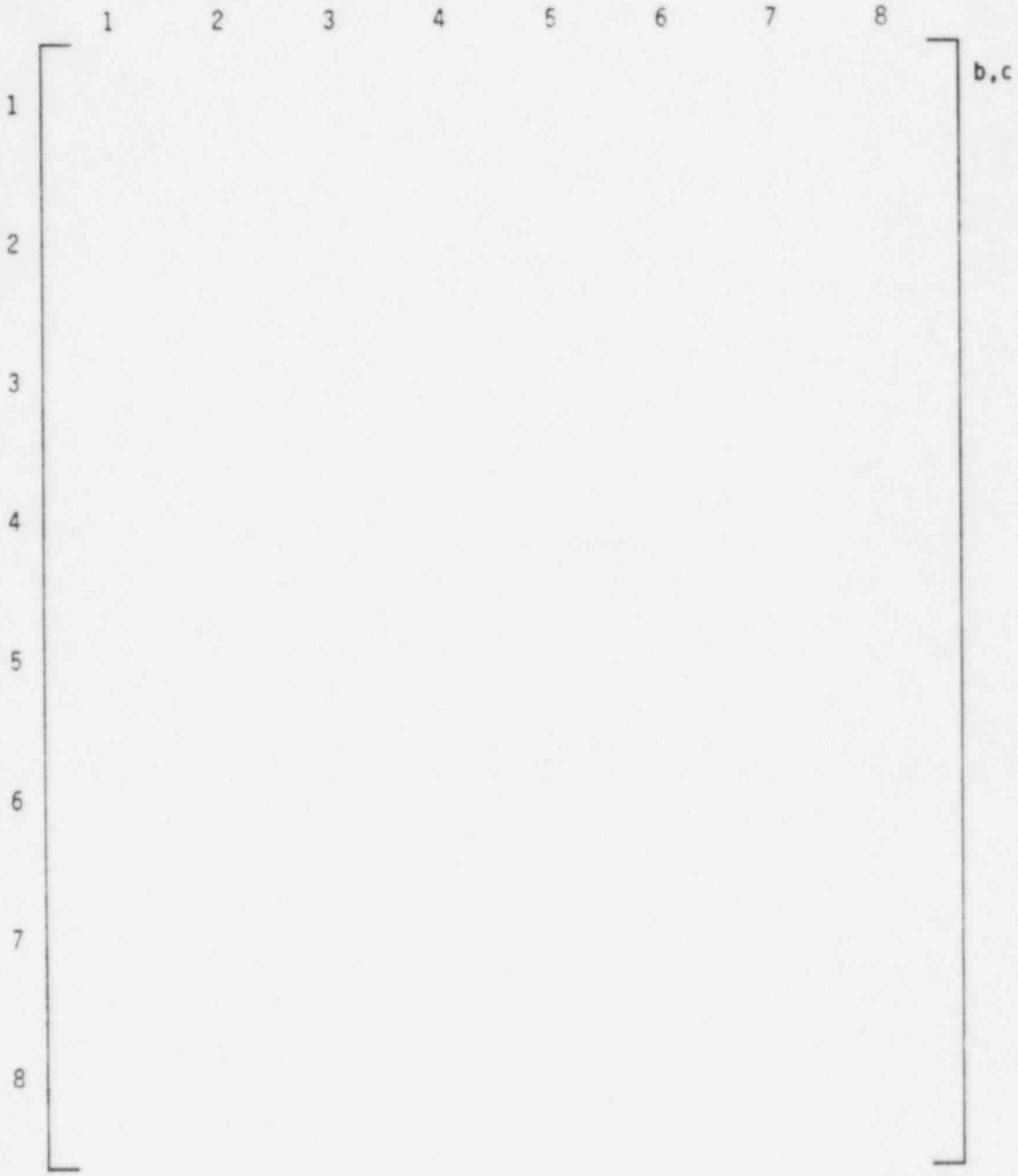

Figure 3-10. Assembly Average Power Comparison
Plant C, Cycle 2, BOL
Normal Operation, ANC/TORTISE

Key: TORTISE
ANC
(ANC - TORTISE) / TORTISE * 100
(ANC - TORTISE)

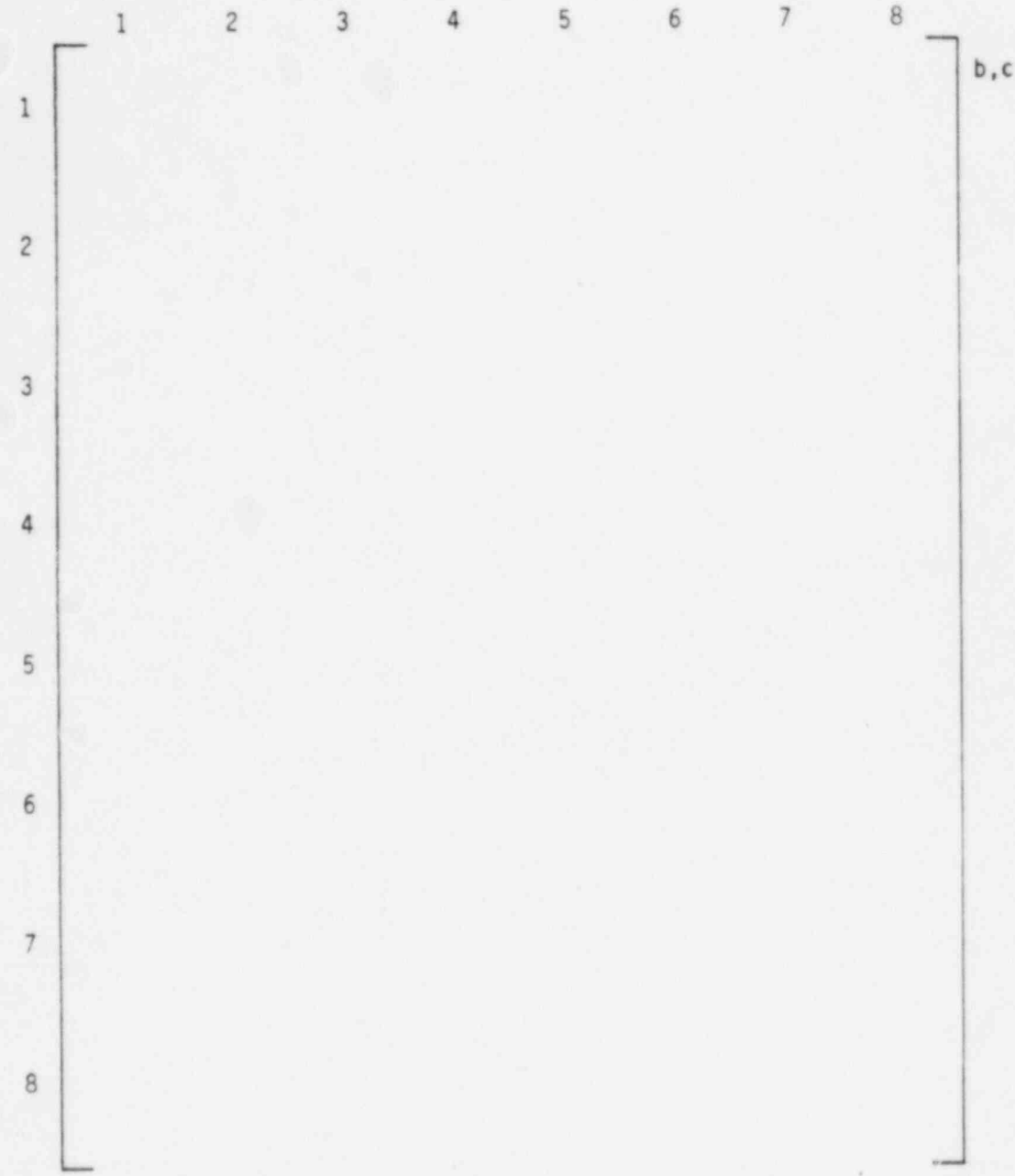

Figure 3-11. Assembly Average Power Comparison
Plant C, Cycle 2, EOL
Normal Operation, ANC/TORTISE

Key: TORTISE
ANC
$\frac{(ANC - TORTISE)}{TORTISE} * 100$

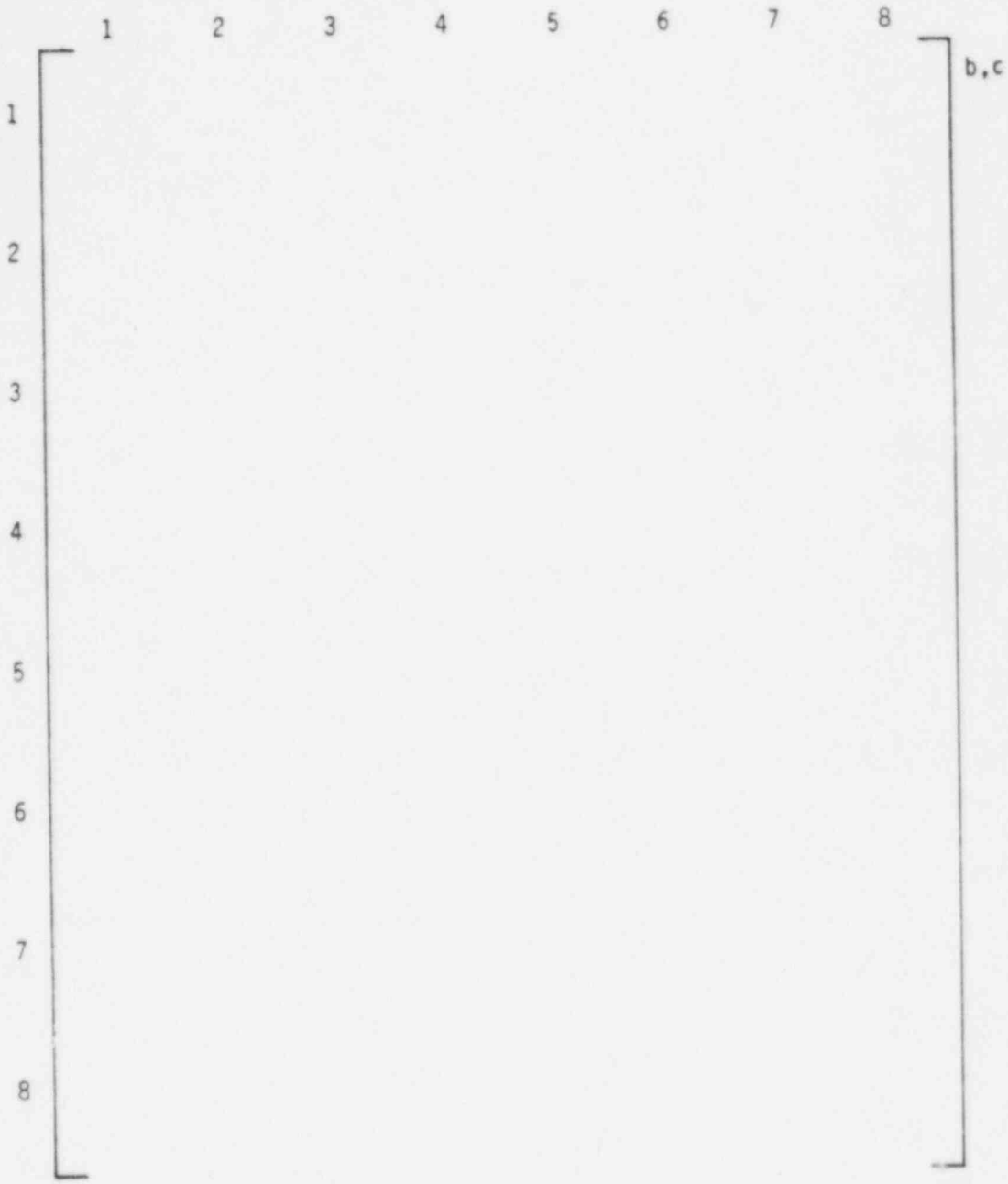

Figure 3-12. Assembly Average Power Comparison
Plant C, Cycle 3, BOL
Normal Operation, ANC/TORTISE

Key: TORTISE
ANC
(ANC - TORTISE) * 100
TORTISE
(ANC - TORTISE)

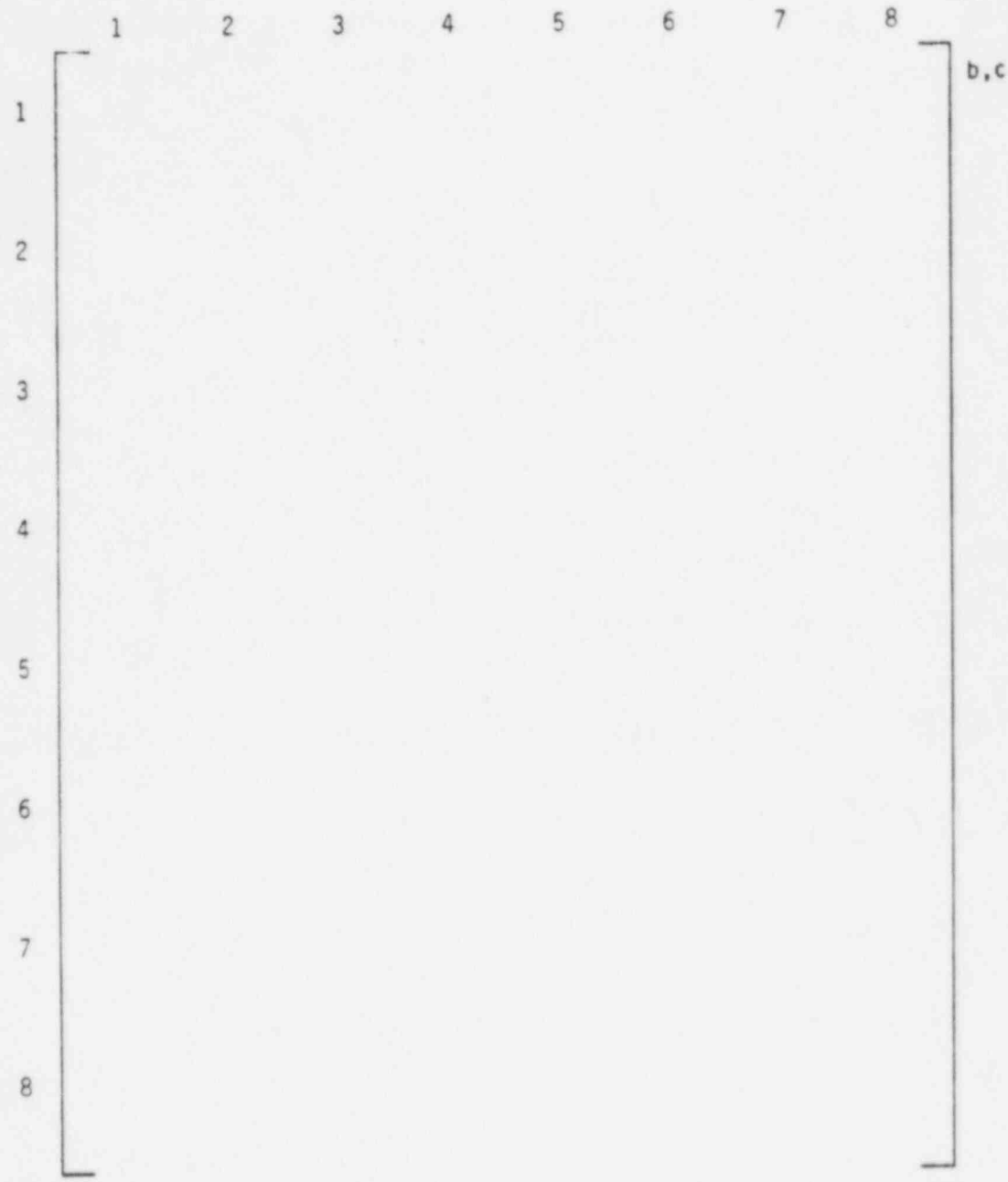

Figure 3-13. Assembly Average Power Comparison
Plant C, Cycle 3, EOL
Normal Operation, ANC/TORTISE

Figures and Tables for Subsection 3-1-3
Rod Power Comparison

TABLE 3-8
PERCENT DIFFERENCE IN ASSEMBLY PEAK POWER AS CALCULATED BY ANC AND TORTISE FOR NORMAL OPERATION

	Mean Difference* (%)	Standard Deviation (%)	N
Total Data Base			
BOL	[		] b,c
EOL			
entire cycle			
Non-BP and Non-Peripheral Assemblies			
BOL	[		] b,c
EOL			
entire cycle			
Non-BP Assemblies			
BOL			
EOL			
entire cycle			
BP Assemblies			
BOL			
EOL			
entire cycle			
Peripheral Assemblies			
BOL			
EOL			
entire cycle	]		]
Non-Peripheral Assemblies			
BOL	[		] b,c
EOL			
entire cycle	]		]

* $\frac{(\text{ANC-TORTISE})}{\text{TORTISE}} * 100\%$

Key: TORTISE
ANC
(ANC - TORTISE) / TORTISE * 100
(ANC - TORTISE)

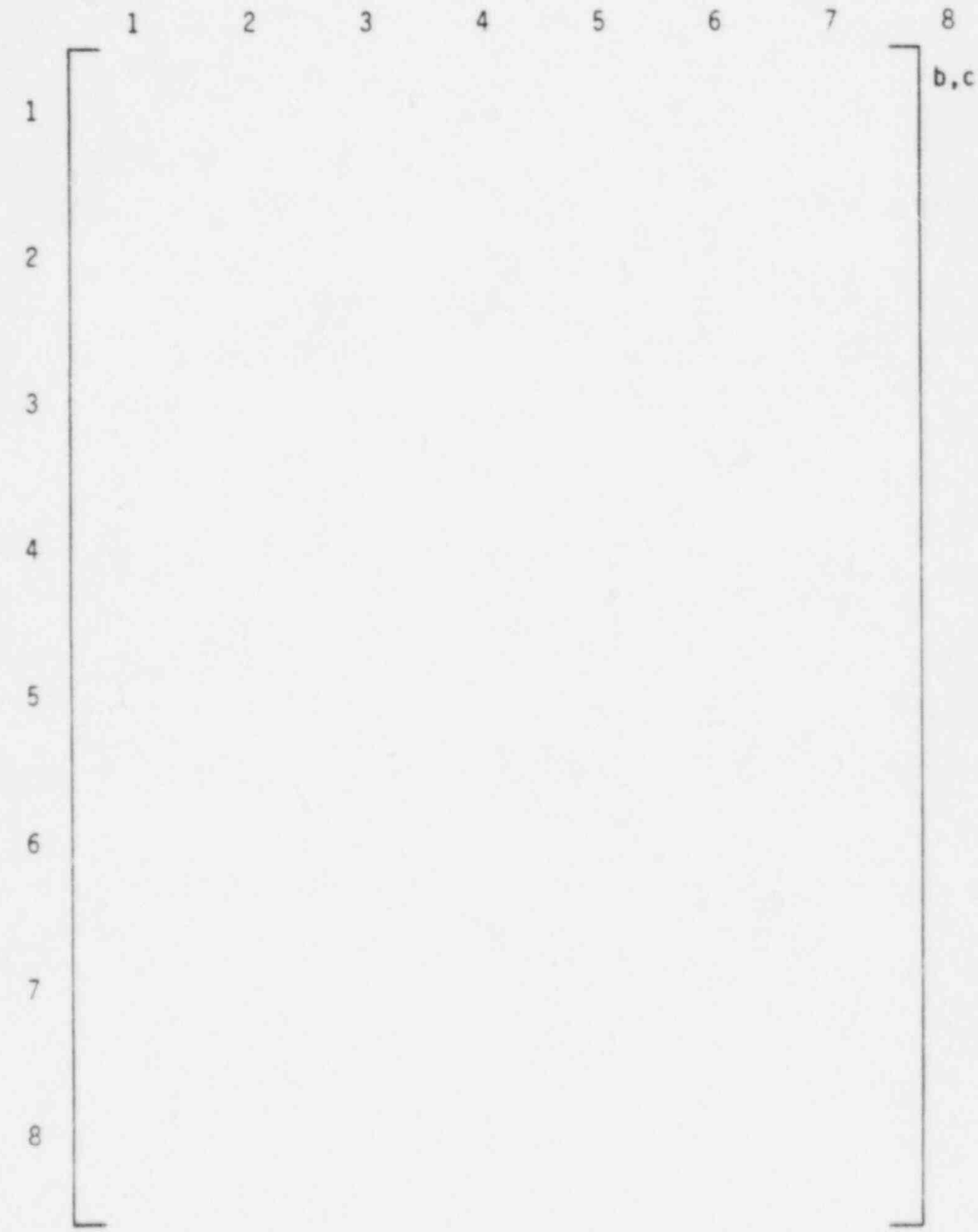

Figure 3-14. ANC/TORTISE Assembly Peak Power Comparison
Plant C, Cycle 1, BOL
Normal Operation

Key:

TORTISE
ANC
(ANC - TORTISE) * 100
TORTISE
(ANC - TORTISE)

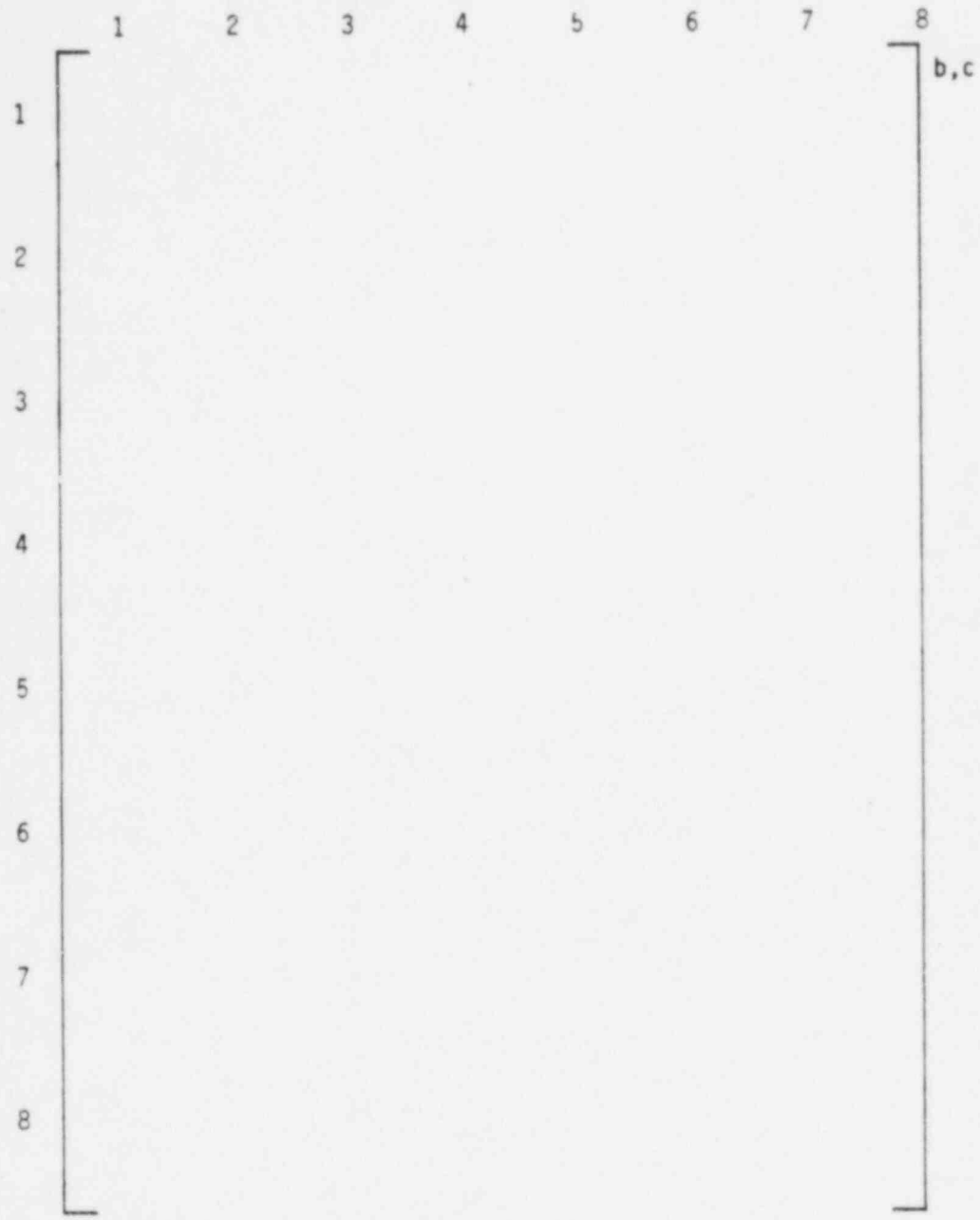

Figure 3-15. ANC/TORTISE Assembly Peak Power Comparison
Plant C, Cycle 1, EOL
Normal Operation

Key: TORTISE
ANC
(ANC - TORTISE) / TORTISE * 100
(ANC - TORTISE)

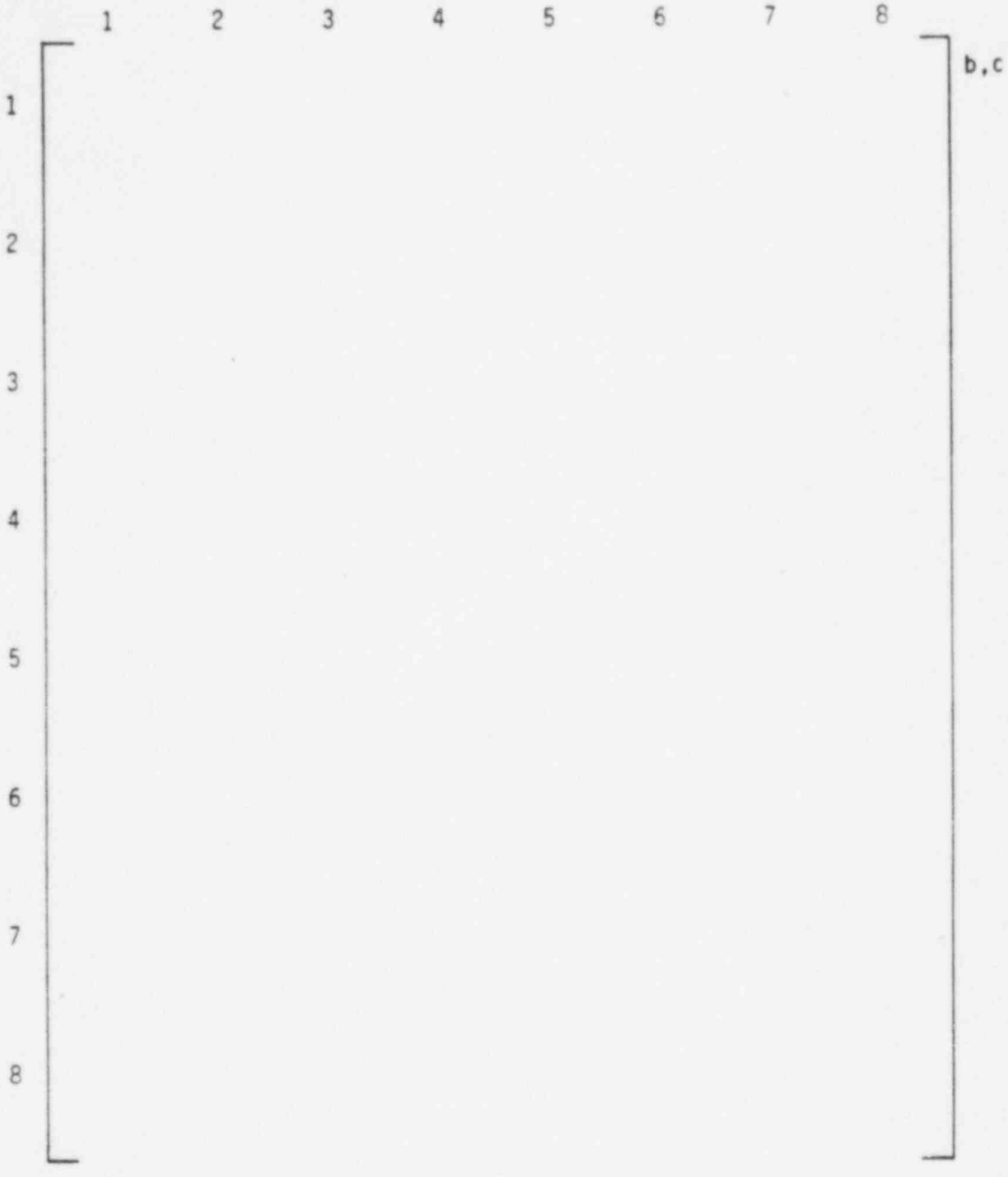

Figure 3-16. ANC/TORTISE Assembly Peak Power Comparison
Plant C, Cycle 2, BOL
Normal Operation

Key: TORTISE
ANC
(ANC - TORTISE) / TORTISE * 100
(ANC - TORTISE)

Figure 3-17. ANC/TORTISE Assembly Peak Power Comparison
Plant C, Cycle 2, EOL
Normal Operation

Key:

TORTISE

ANC

$$\frac{(\text{ANC} - \text{TORTISE})}{\text{TORTISE}} * 100$$

(ANC - TORTISE)

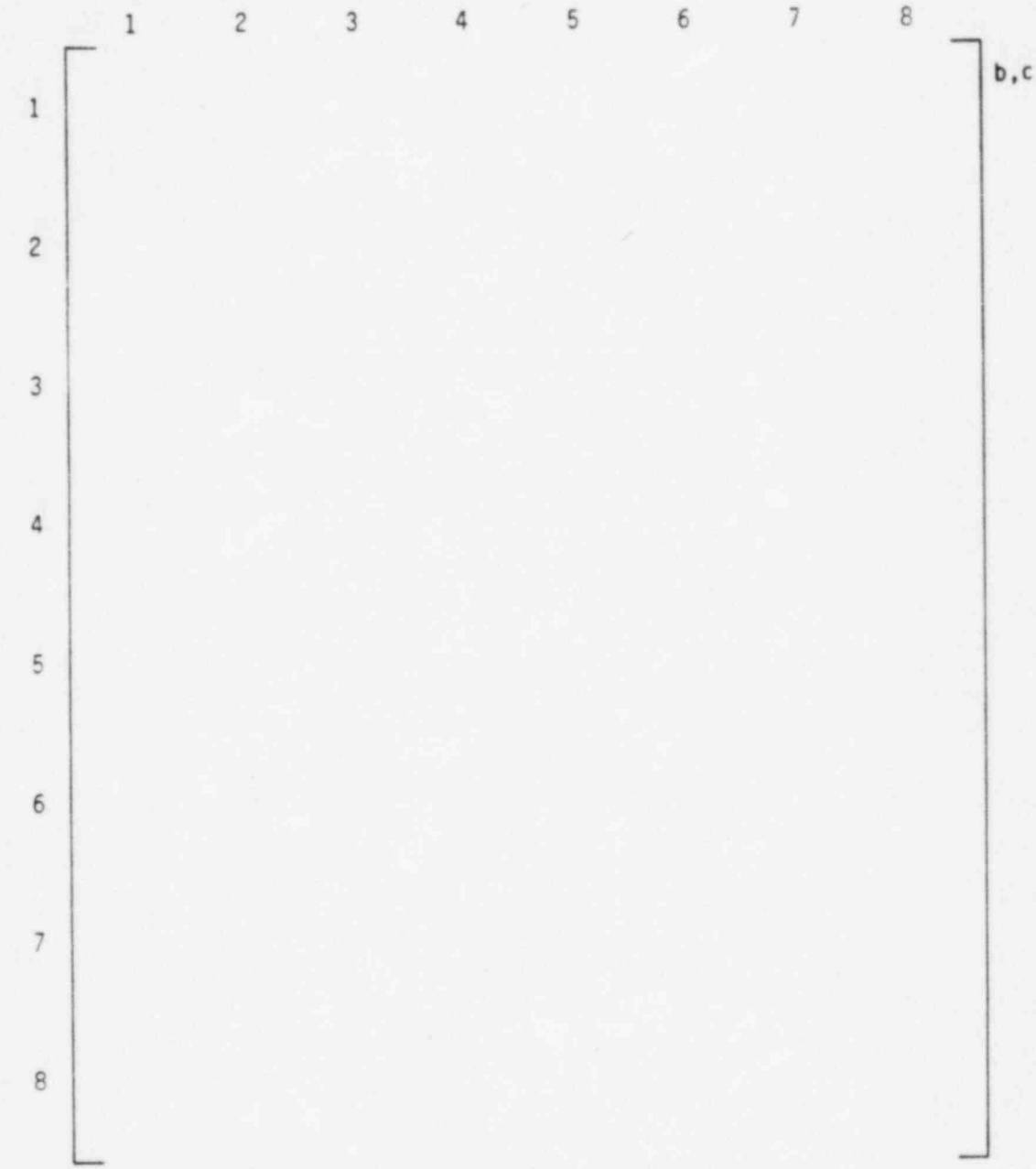

Figure 3-18. ANC/TORTISE Assembly Peak Power Comparison
Plant C, Cycle 3, BOL
Normal Operation

Key: TORTISE
ANC
(ANC - TORTISE) / TORTISE * 100
(ANC - TORTISE)

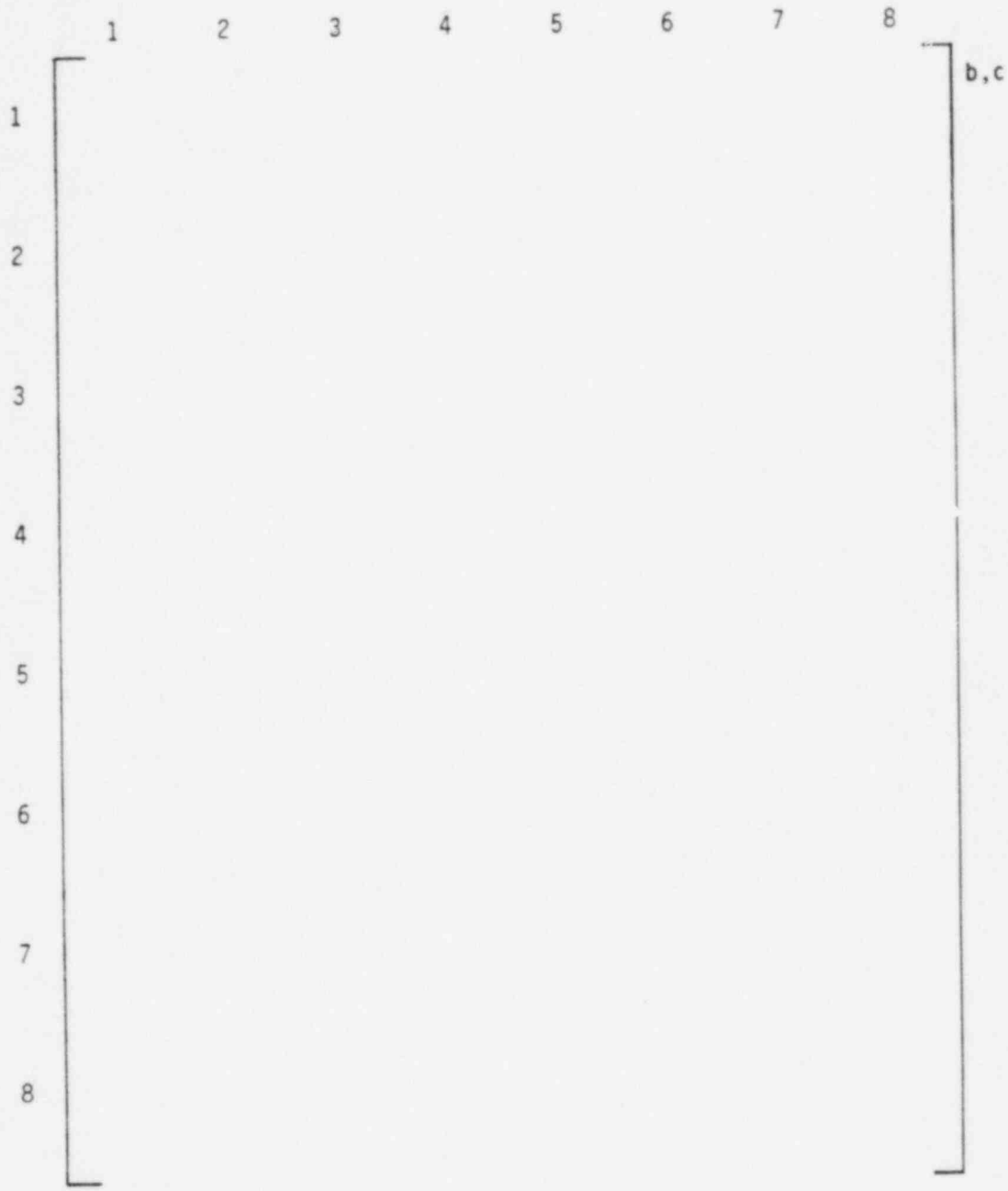

Figure 3-19. ANC/TORTISE Assembly Peak Power Comparison
Plant C, Cycle 3, EOL
Normal Operation

TABLE 3-9
PERCENT DIFFERENCE IN CORE PEAK POWER AS CALCULATED
BY ANC AND TORTISE FOR NORMAL OPERATION

Plant	Mean Difference (%)	Standard Deviation (%)	N	
Plant A, Cycle 8	[			] b,c
Plant B, Cycle 1				
Plant C, Cycle 1				
Plant C, Cycle 2				
Plant C, Cycle 3				
total database				]

$$\frac{(\text{ANC}-\text{TORTISE})}{\text{TORTISE}} * 100$$

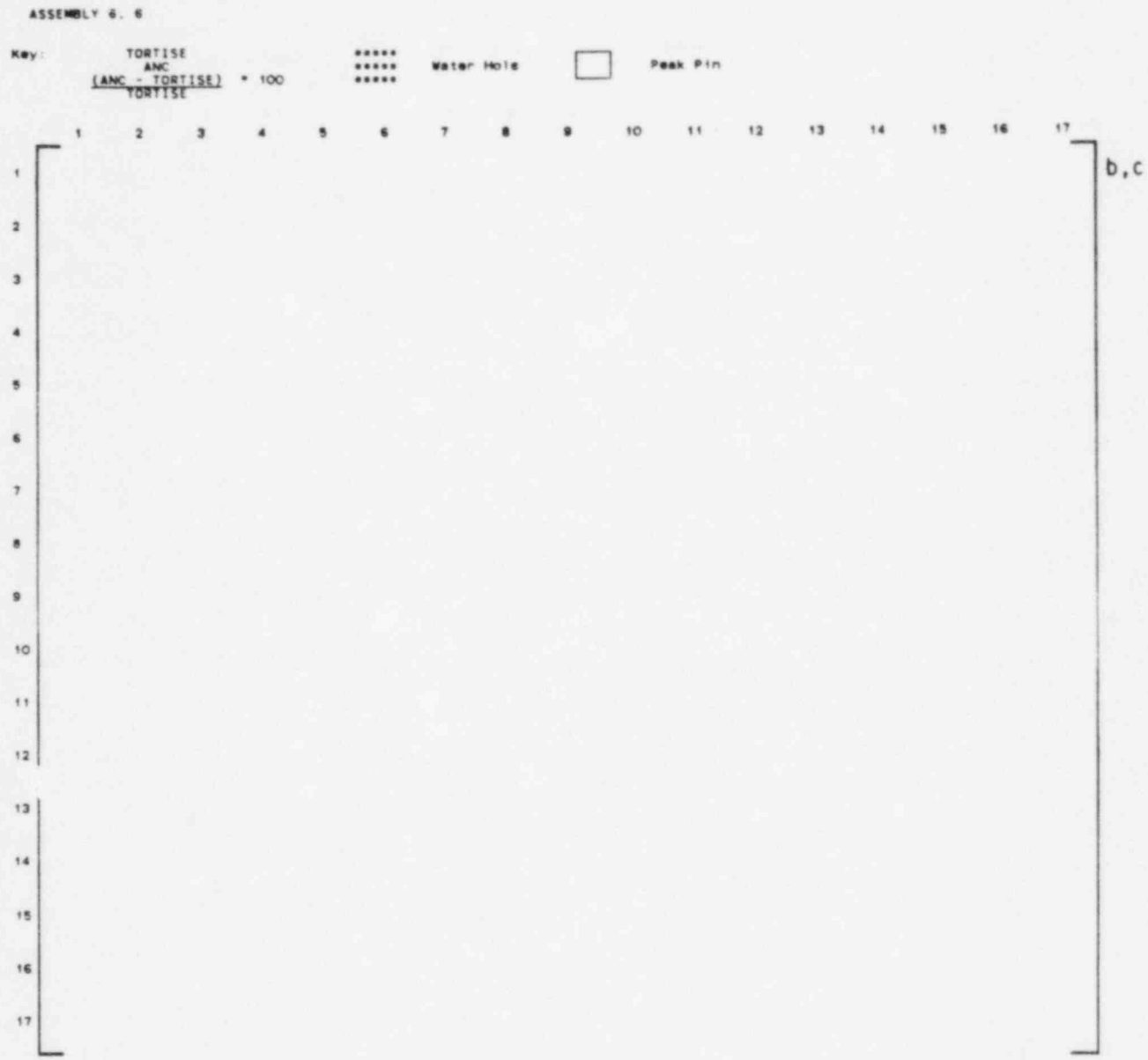

Figure 3-20. Assembly Rod Power, ANC/TORTISE Comparison
Plant C, Cycle 3, Assembly (6,6)

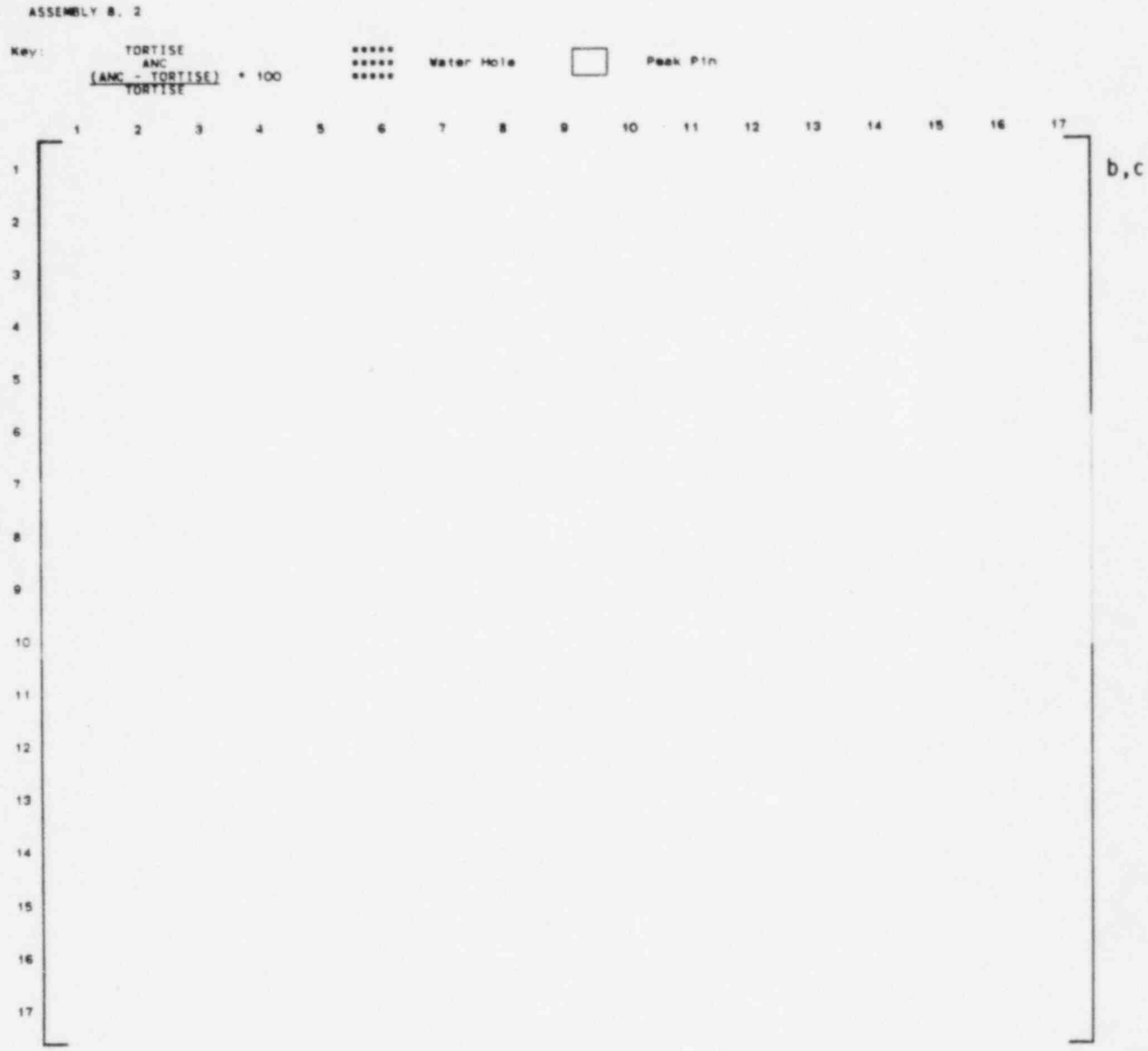

Figure 3-21. Assembly Rod Power, ANC/TORTISE Comparison
Plant C, Cycle 3, Assembly (8,2)

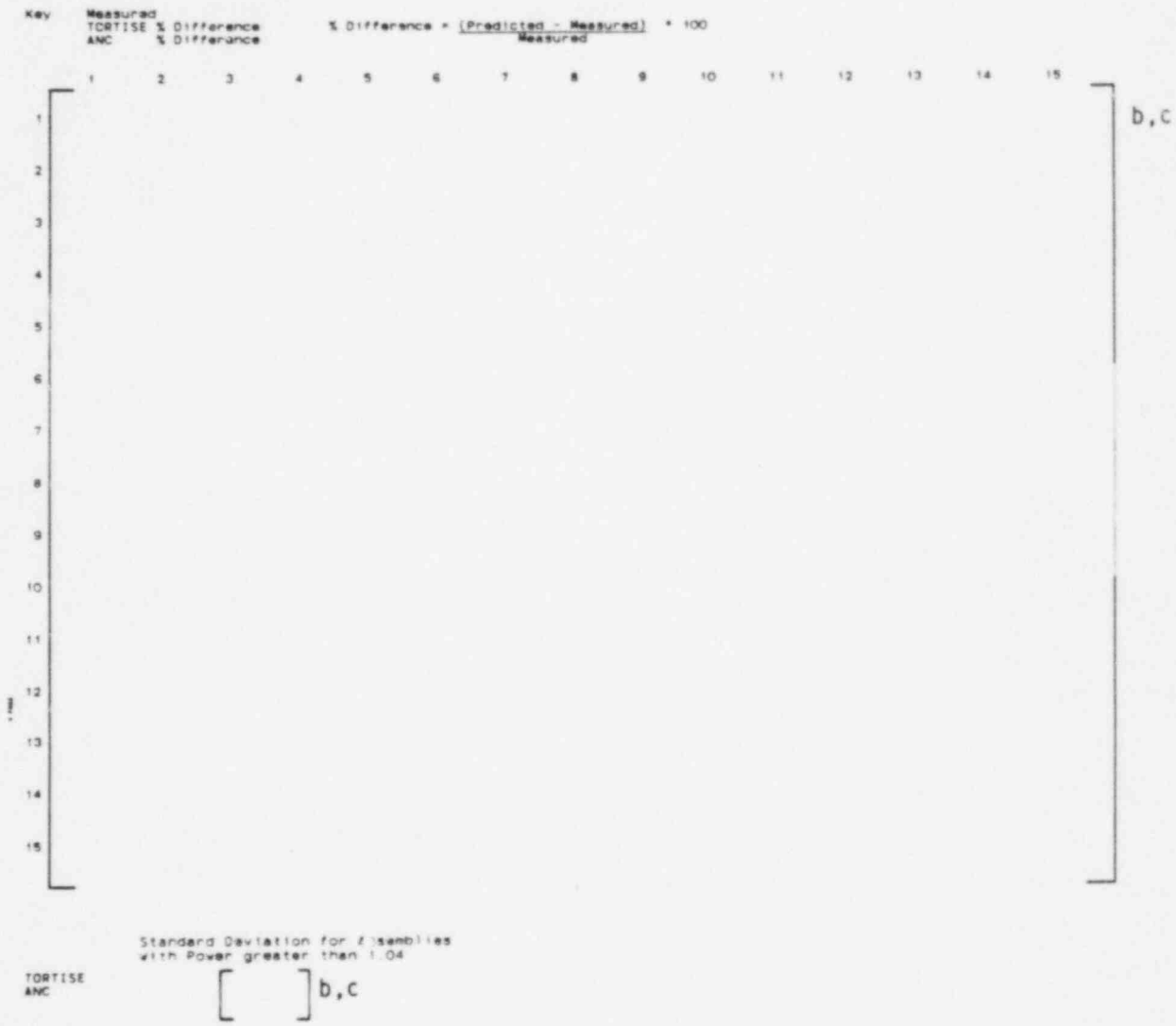

Figure 3-22. Measured and Predicted Reaction Rate Integrals Plant C, Cycle 2, 11,000 MWD/MTU

Figures and Tables for Subsection 3-1-4
Axial Power Distribution

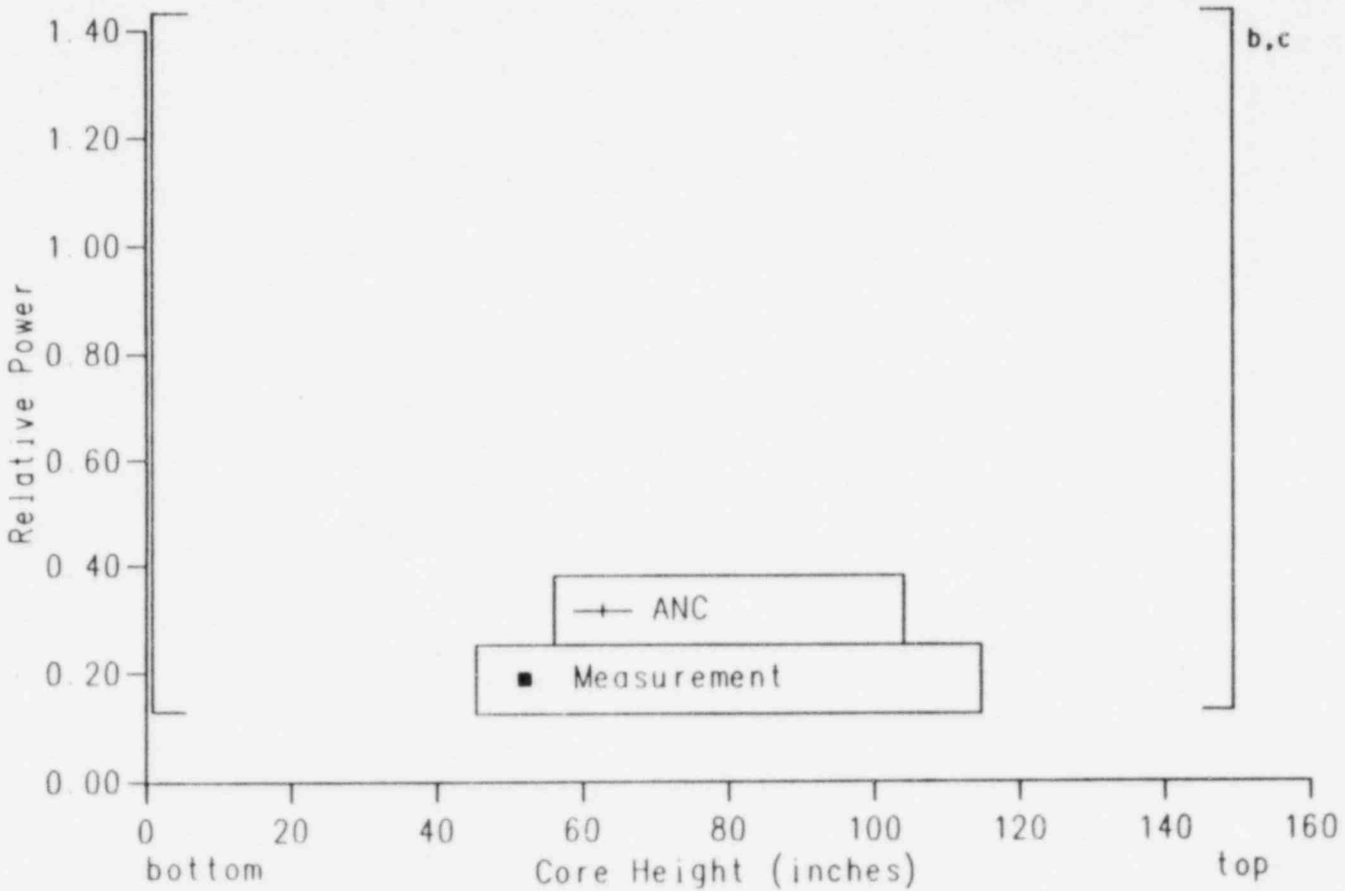

Figure 3-23. ANC and Measurement Comparison
Core Average Axial Power Shape
Plant C, Cycle 1, ARO, 1,000 MWD/MTU

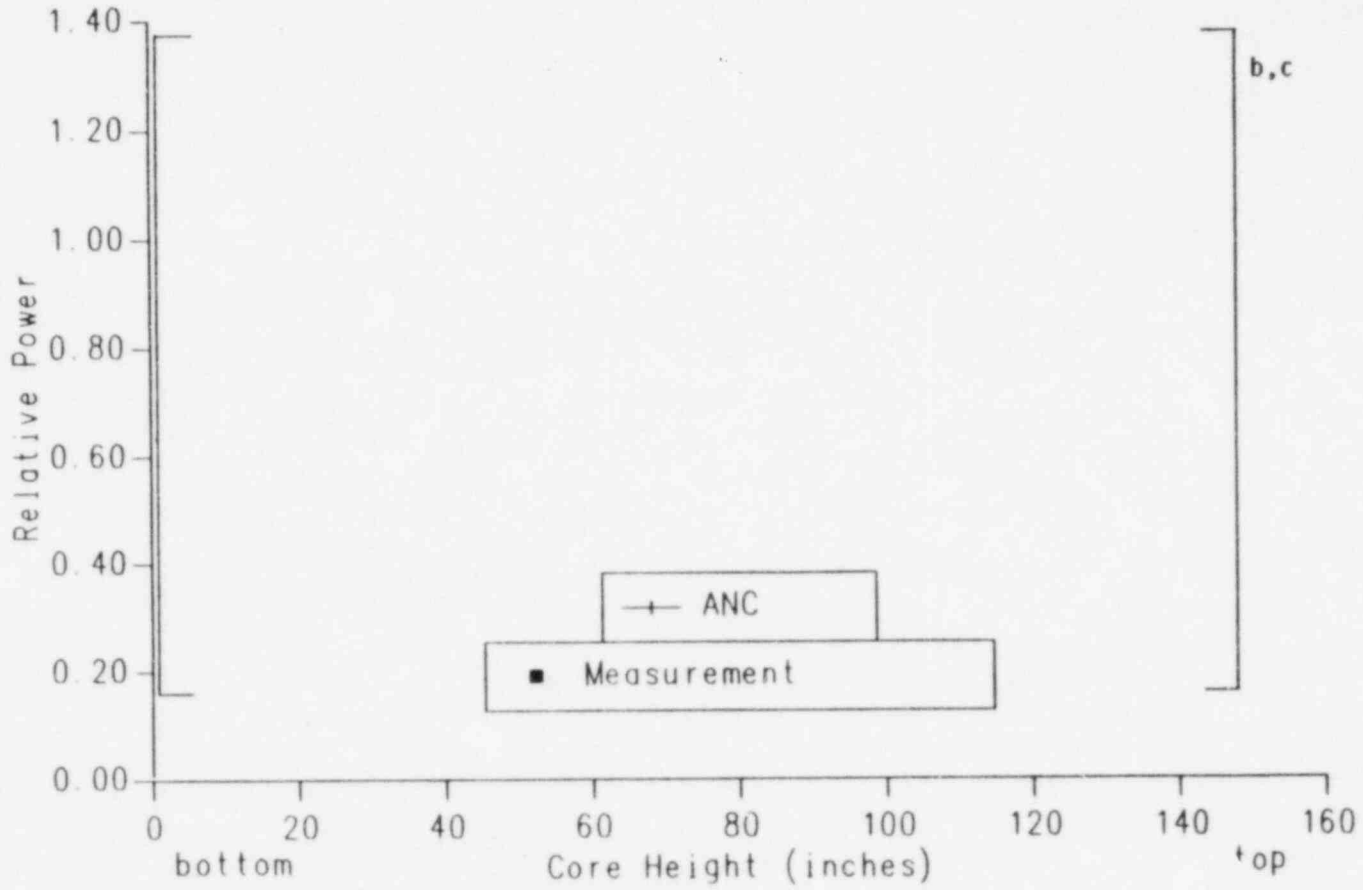

Figure 3-24. ANC and Measurement Comparison
Core Average Axial Power Shape
Plant C, Cycle 1, ARO, 3,000 MWD/MTU

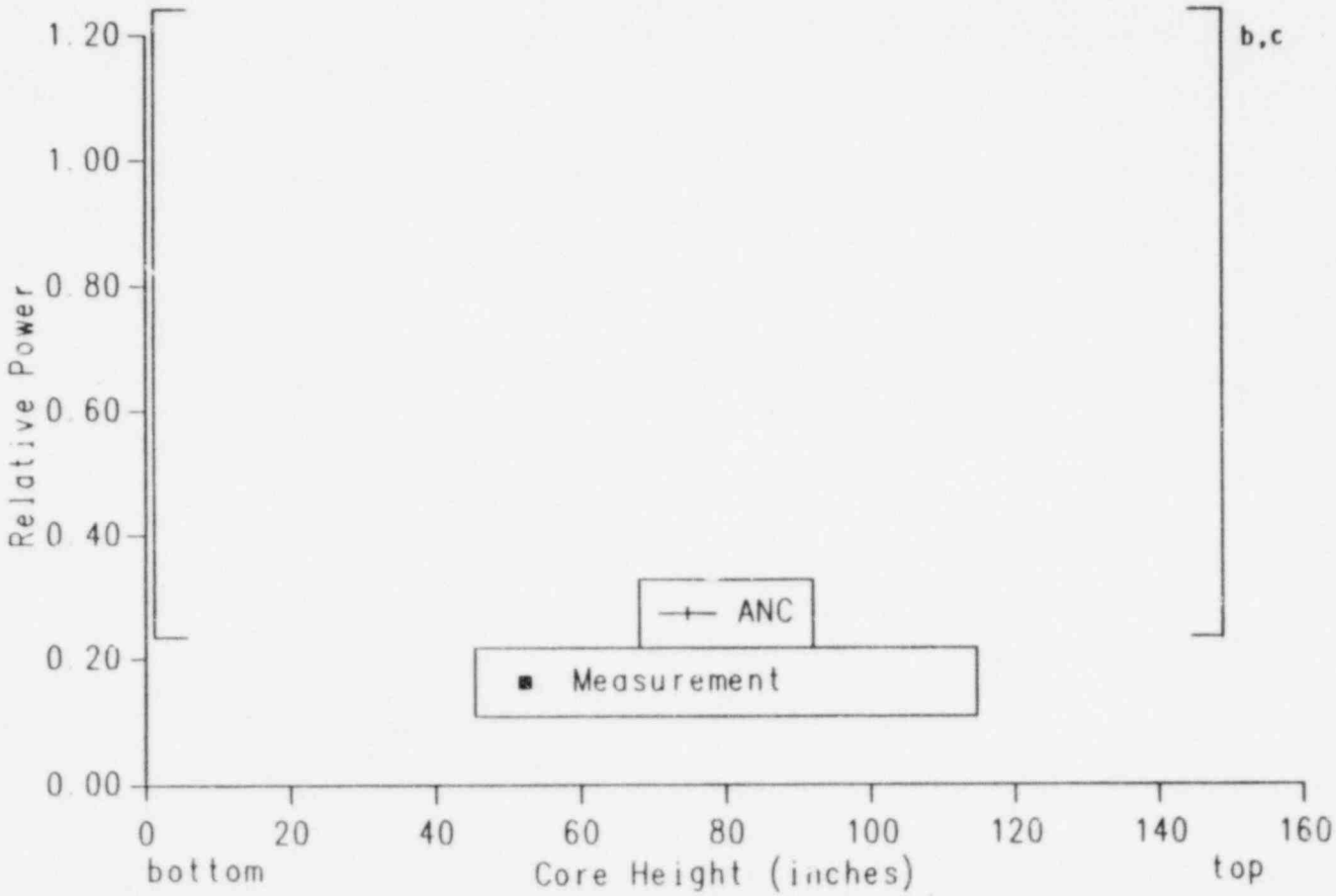

Figure 3-25. ANC and Measurement Comparison
Core Average Axial Power Shape
Plant C, Cycle 1, ARO, 6,000 MWD/MTU

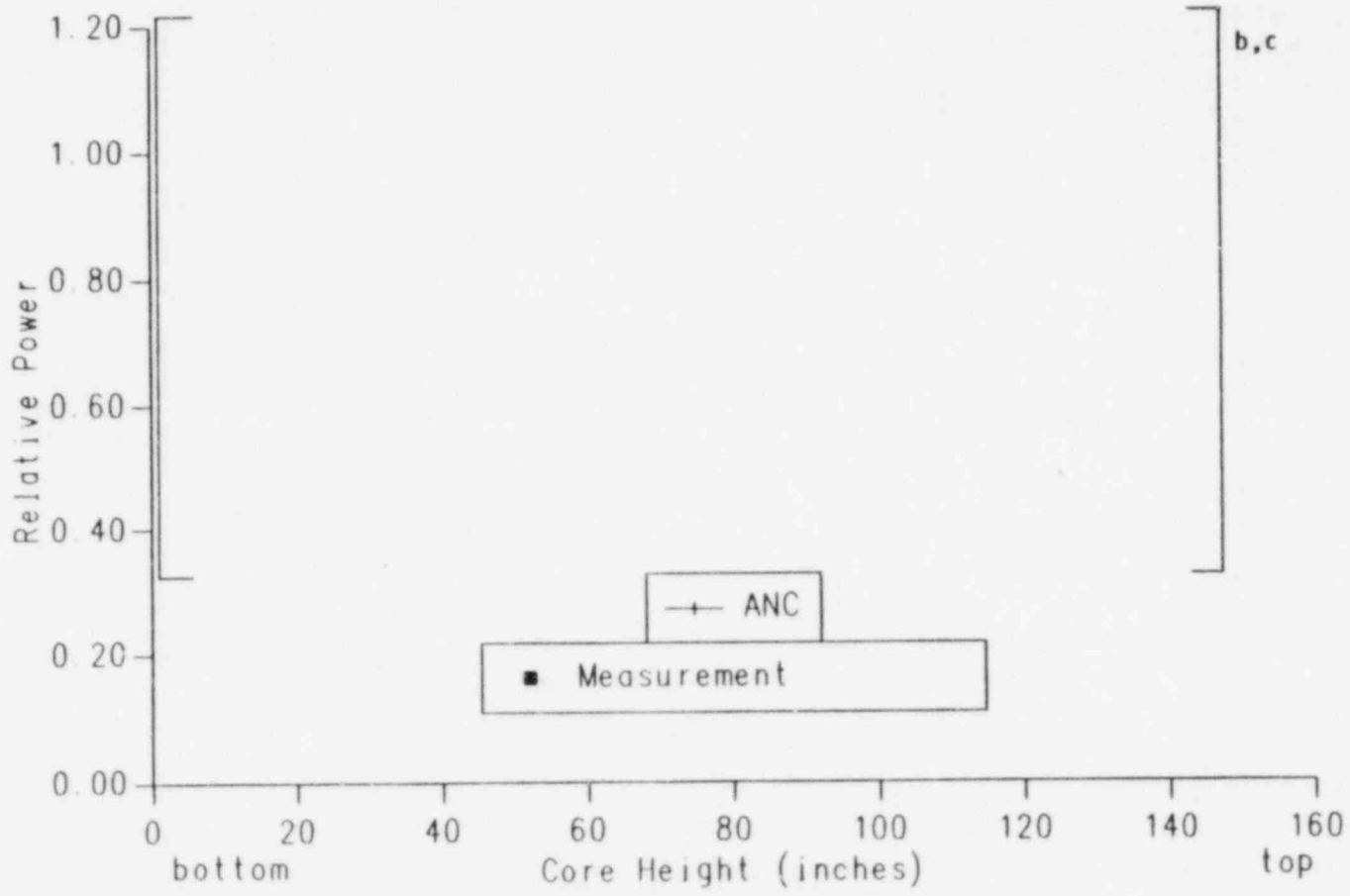

Figure 3-26. ANC and Measurement Comparison
Core Average Axial Power Shape
Plant C, Cycle 1, ARO, 10,000 MWD/MTU

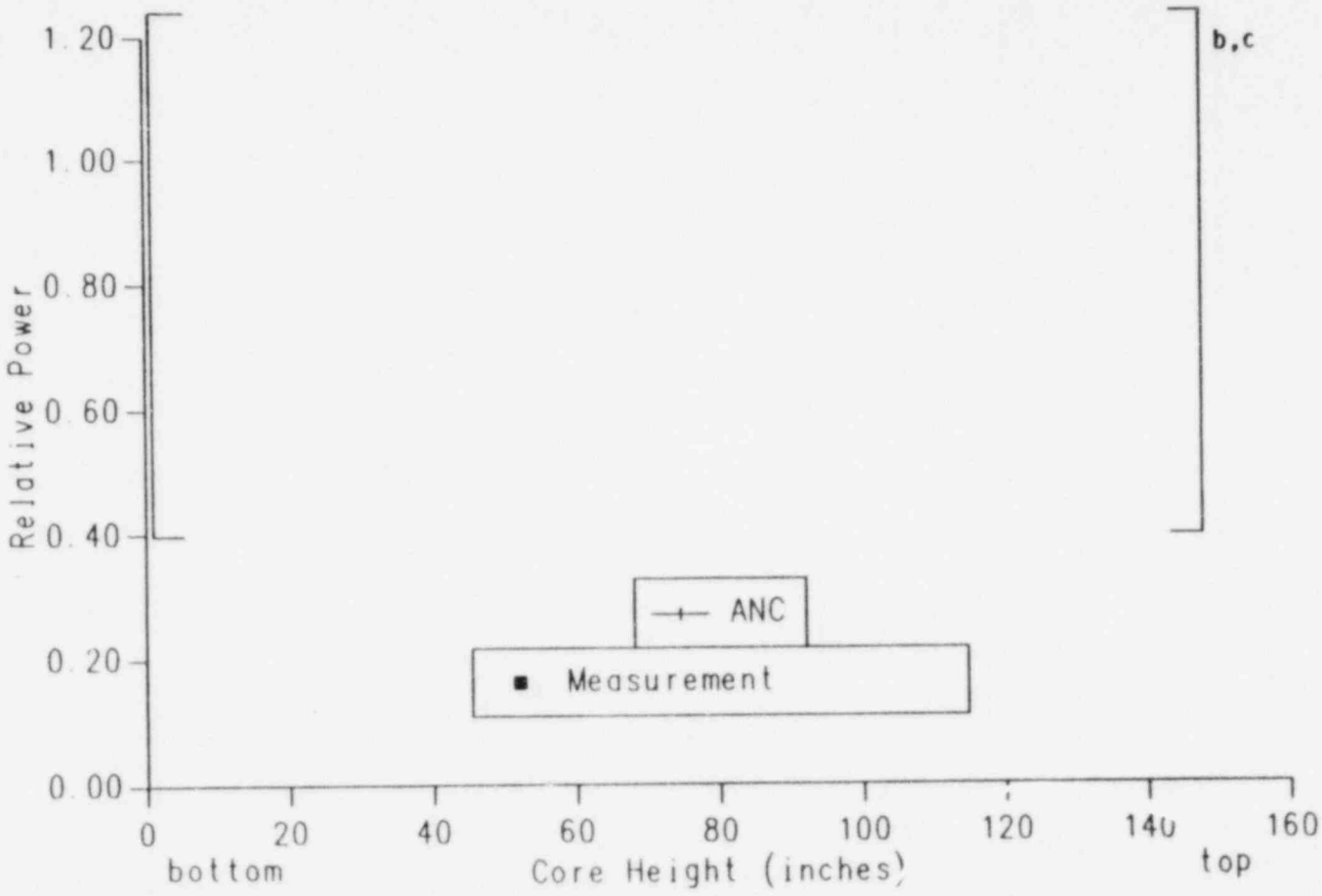

Figure 3-27. ANC and Measurement Comparison
Core Average Axial Power Shape
Plant C, Cycle 1, ARO, 14,000 MWD/MTU

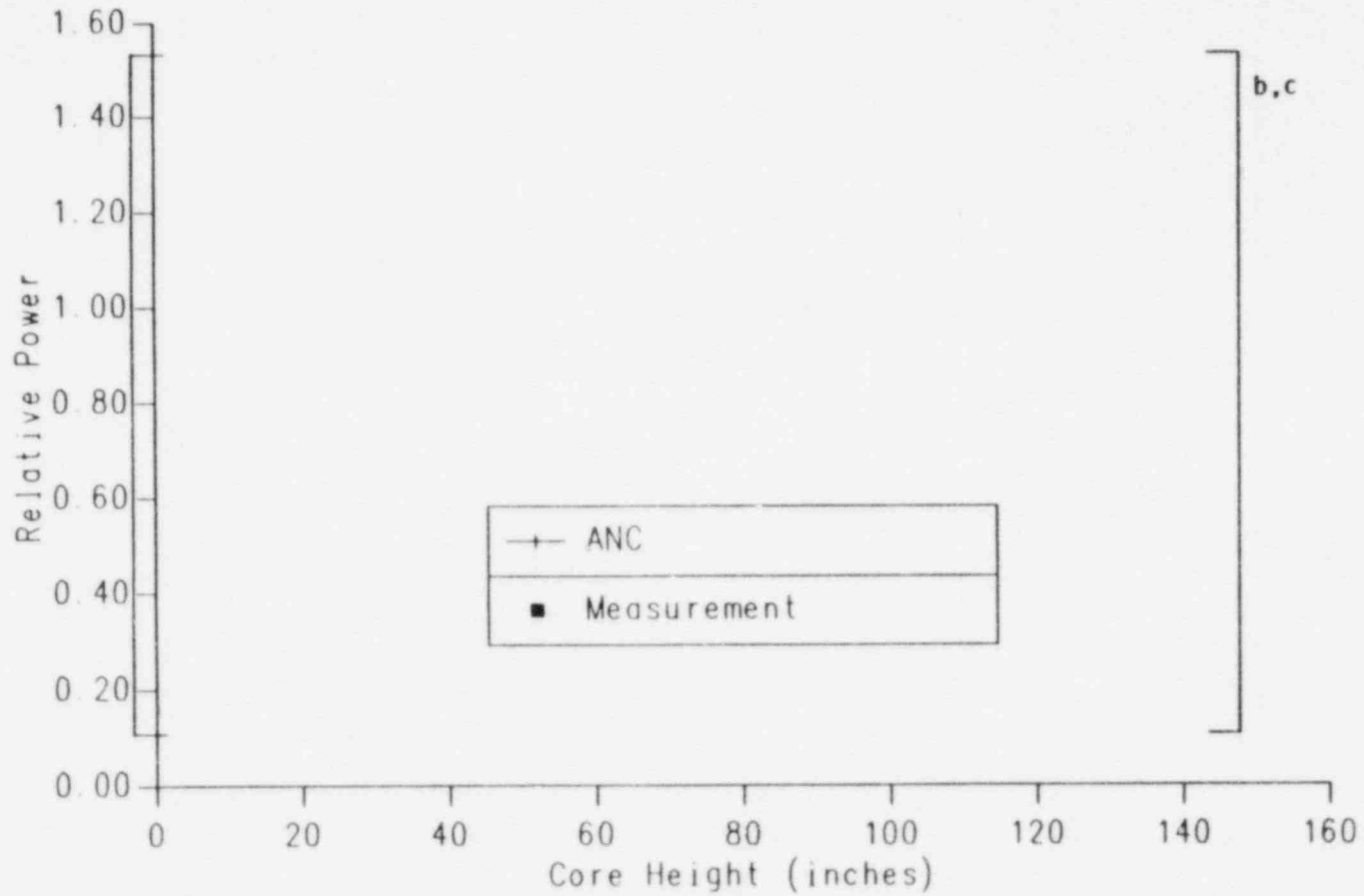

Figure 3-28. ANC and Measurement Comparison
Core Average Axial Power Shape
Plant C, Cycle 1, D-In HZP, Zero MWD/MTU

TABLE 3-10
MEASUREMENT AND ANC AXIAL OFFSET COMPARISON
PLANT C, CYCLE 1

Cycle Burnup (MWD/MTU)	INCORE (%)	ANC (%)
1000	[	] a,c
3000		
6000		
10000		
14000		

Figures and Table for Subsection 3-1-5
Reactivity Coefficients

TABLE 3-11
ANC AND TORTISE COMPARISON
MODERATOR TEMPERATURE COEFFICIENT
(pcm/°F)

Plant	Condition	TORTISE	ANC	ANC - TORTISE
Plant A, Cycle 8	[			] b,c
Plant B, Cycle 1				
Plant C, Cycle 1				
Plant C, Cycle 2				
Plant C, Cycle3				

TABLE 3-12
ANC AND TORTISE COMPARISON OF BORON COEFFICIENTS
(pcm/ppm)

Plant	Condition	TORTISE	ANC	ANC - TORTISE
Plant A, Cycle 8	[			] b,c
Plant B, Cycle 1				
Plant C, Cycle 1				
Plant C, Cycle 2				
Plant C, Cycle 3				

Figures and Tables for Subsection 3-1-6
Control Rod Worths

TABLE 3-13
ANC AND TORTISE COMPARISON OF CONTROL ROD WORTHS

Condition	Rod Configuration	TORTISE	ANC	Percent* Difference
Plant A, Cycle 8	[			] b,c
Plant B, Cycle 1	[			] b,c
Plant C, Cycle 1	[			] b,c
Plant C, Cycle 3	[			] b,c

$$* \frac{(ANC - TORTISE)}{TORTISE} * 100$$

TABLE 3-14
SUMMARY OF ANC AND TORTISE COMPARISON
OF CONTROL ROD WORTHS

Condition	Rod Configuration	Mean Difference (%)	Standard Deviation (%)	N
BOL-HZP	[			] b,c
Total Database	[			] b,c

Figures and Tables for Subsection 3-2-1
Rod Ejection

TABLE 3-15
SUMMARY OF ANC AND TORTISE CALCULATIONS
OFF-NORMAL OPERATION -- EJECTED ROD

	Plant B Cycle 1	Plant C Cycle 1	Plant C Cycle 2	Plant C Cycle 3	Mean	Standard Deviation
Condition	BOL HFP	EOL HZP	EOL HZP	EOL HZP		
Rod Worth (pcm)						
TORTISE	[					] b,c
ANC						
Percent Difference						
Maximum Assembly Average Power						
TORTISE						
ANC						
Percent Difference						
Maximum Assembly Peak Power						
TORTISE						
ANC						
Percent Difference						

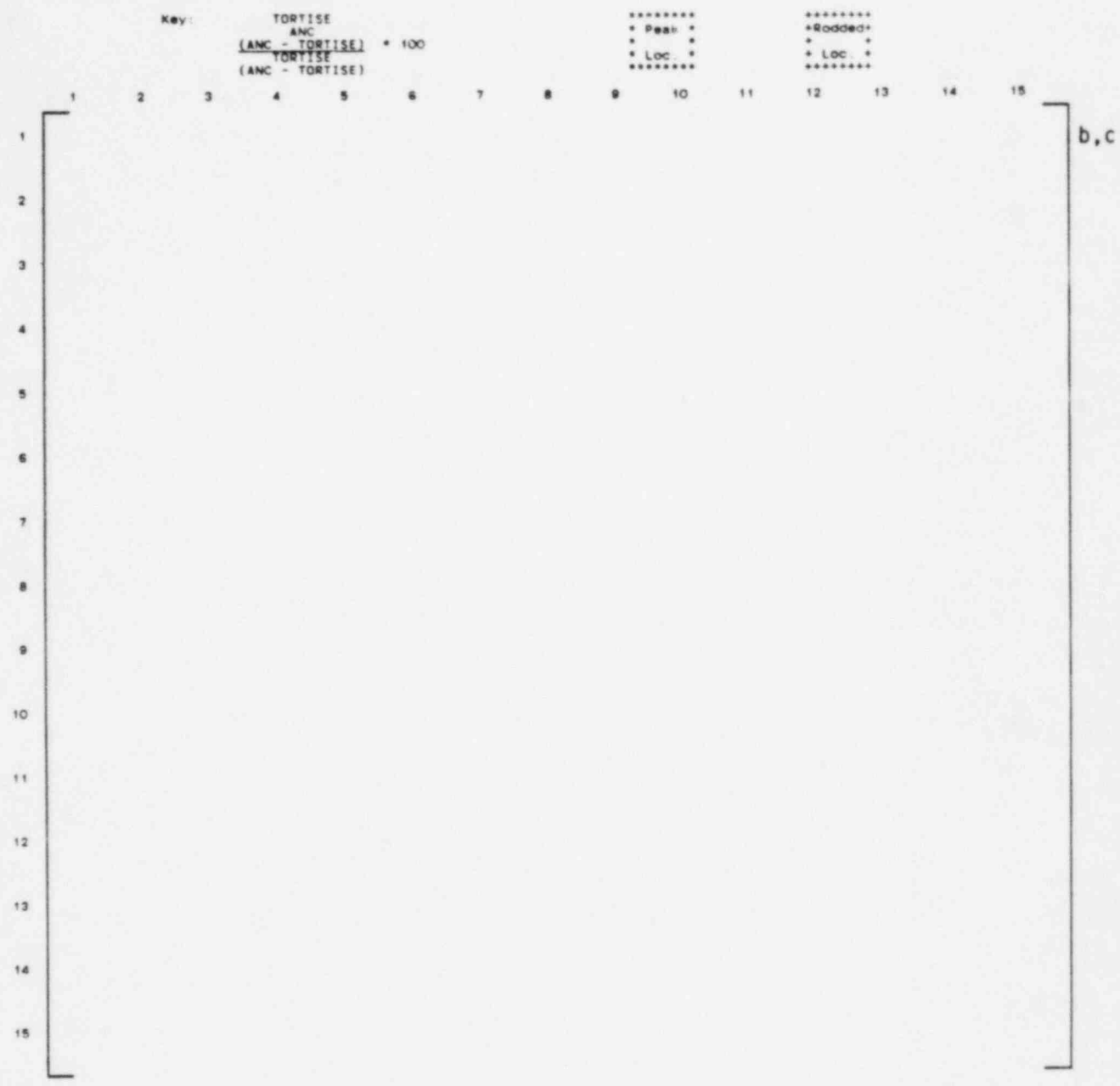

Figure 3-29. ANC/TORTISE Assembly Average Power Comparison
Plant B, Cycle 1, BOL, HFP
Off-Normal Operation -- Ejected Rod

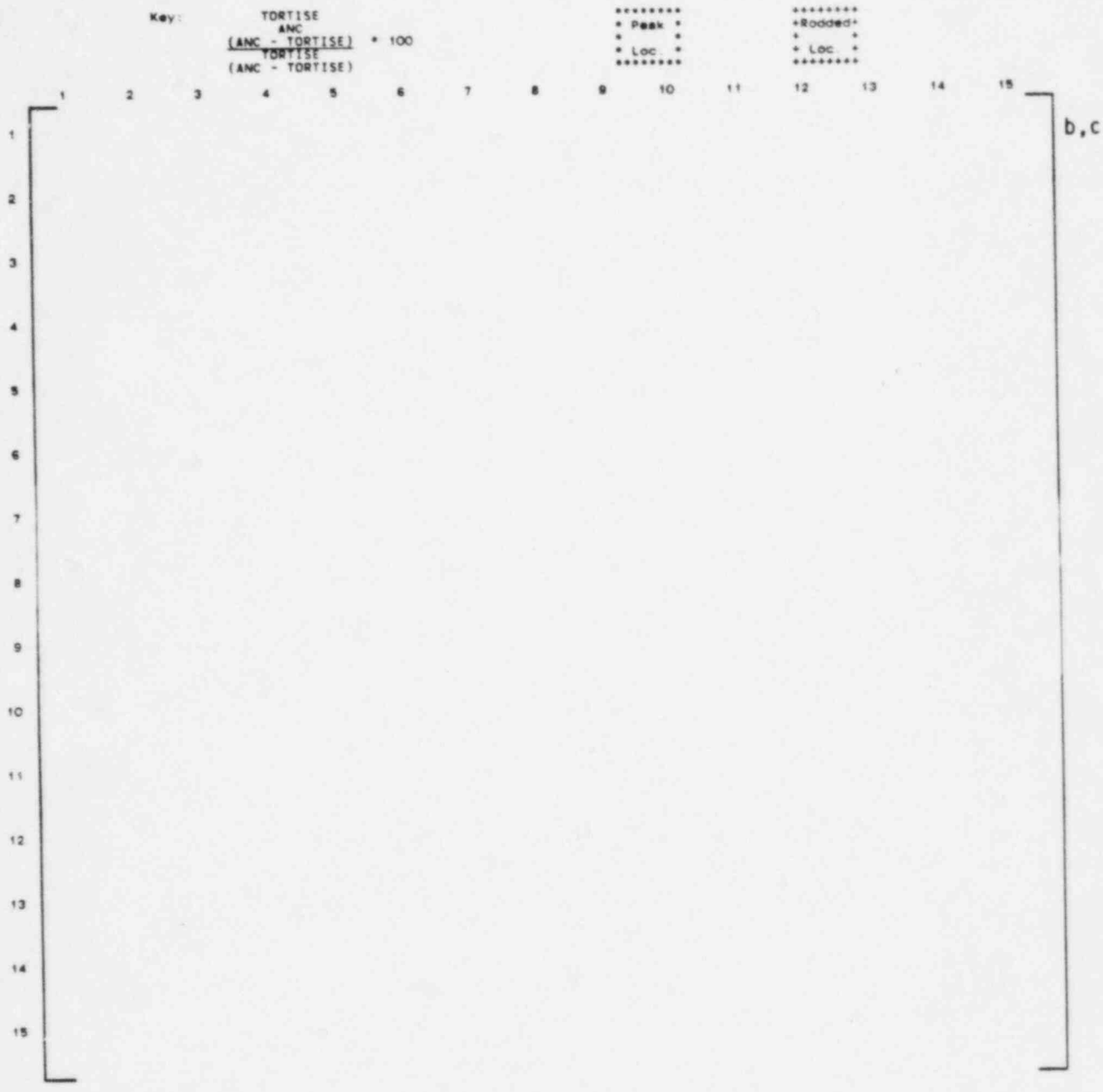

Figure 3-30. ANC/TORTISE Assembly Average Power Comparison
Plant C, Cycle 1, EOL, HZP
Off-Normal Operation -- Ejected Rod

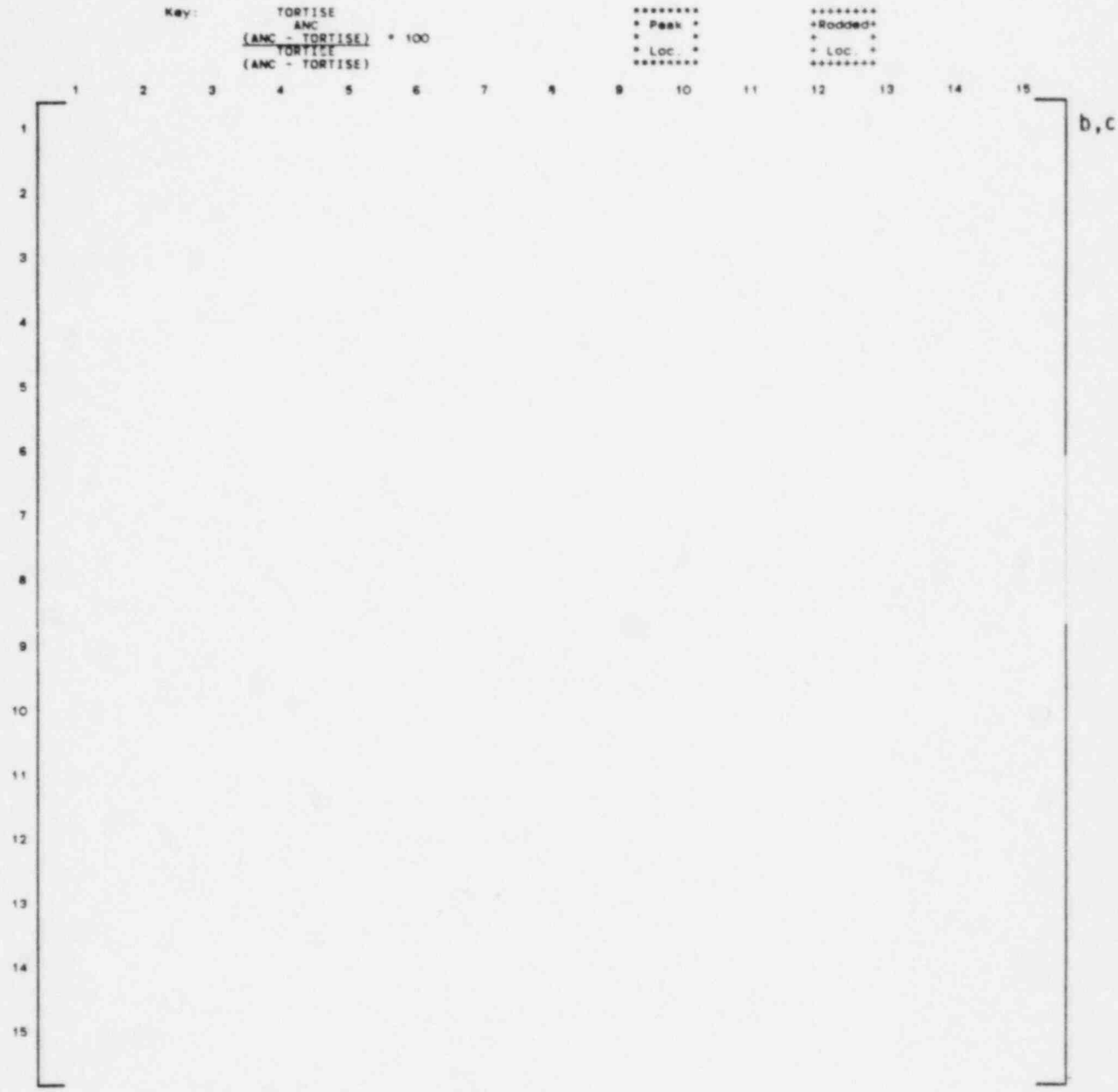

Figure 3-31. ANC/TORTISE Assembly Average Power Comparison
Plant C, Cycle 2, EOL, HZP
Off-Normal Operation -- Ejected Rod

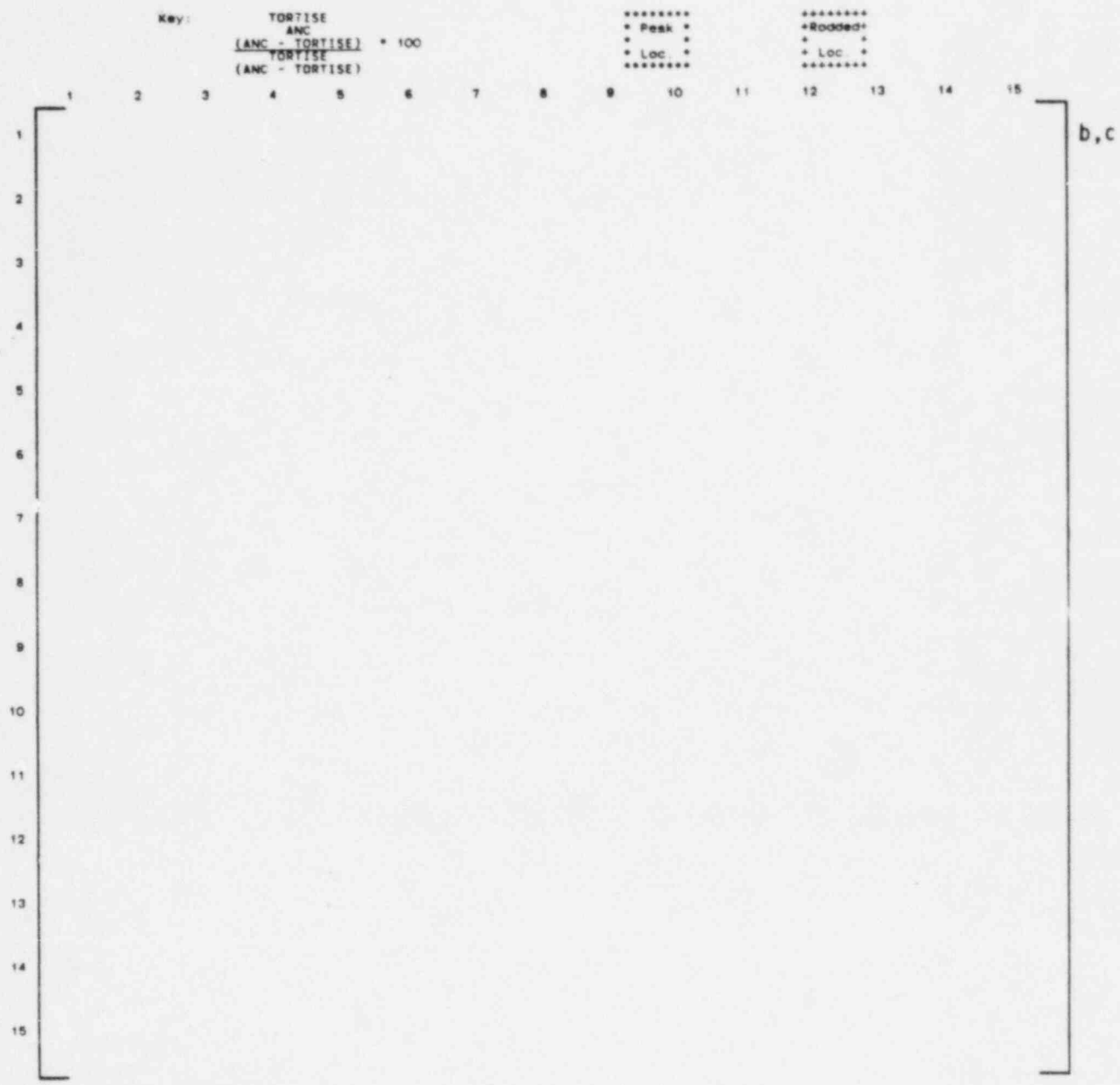

Figure 3-32. ANC/TORTISE Assembly Average Power Comparison
Plant C, Cycle 3, EOL, HZP
Off-Normal Operation -- Ejected Rod

Figure 3-33. ANC/TORTISE Assembly Peak Power Comparison
Plant C, Cycle 2, EOL, HZP
Off-Normal Operation -- Ejected Rod

Figures and Tables for Subsection 3-2-2
Stuck Rod

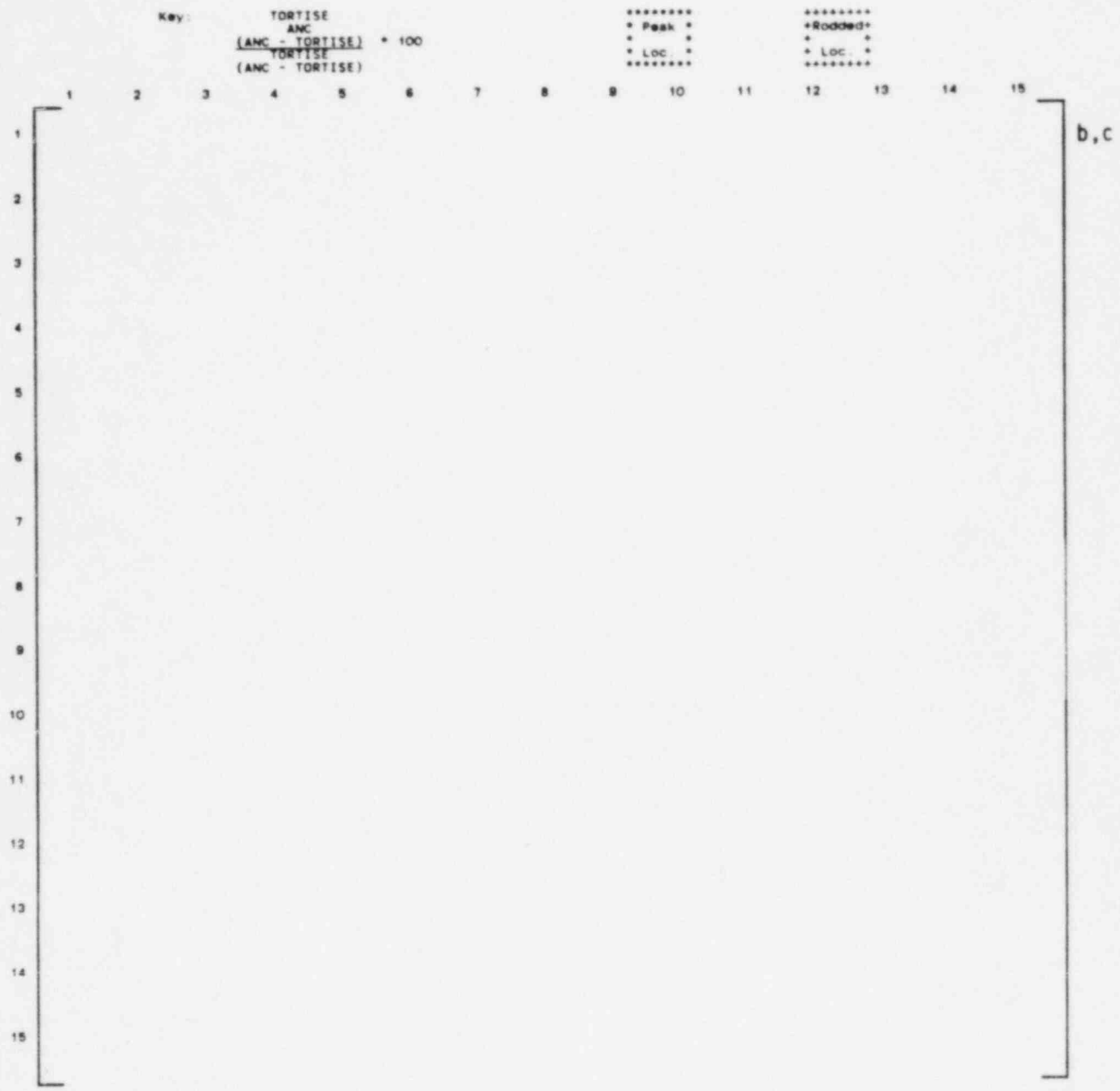

Figure 3-34. ANC/TORTISE Assembly Average Power Comparison
Plant C, Cycle 1, EOL, HZP
Off-Normal Operation -- Stuck Rod

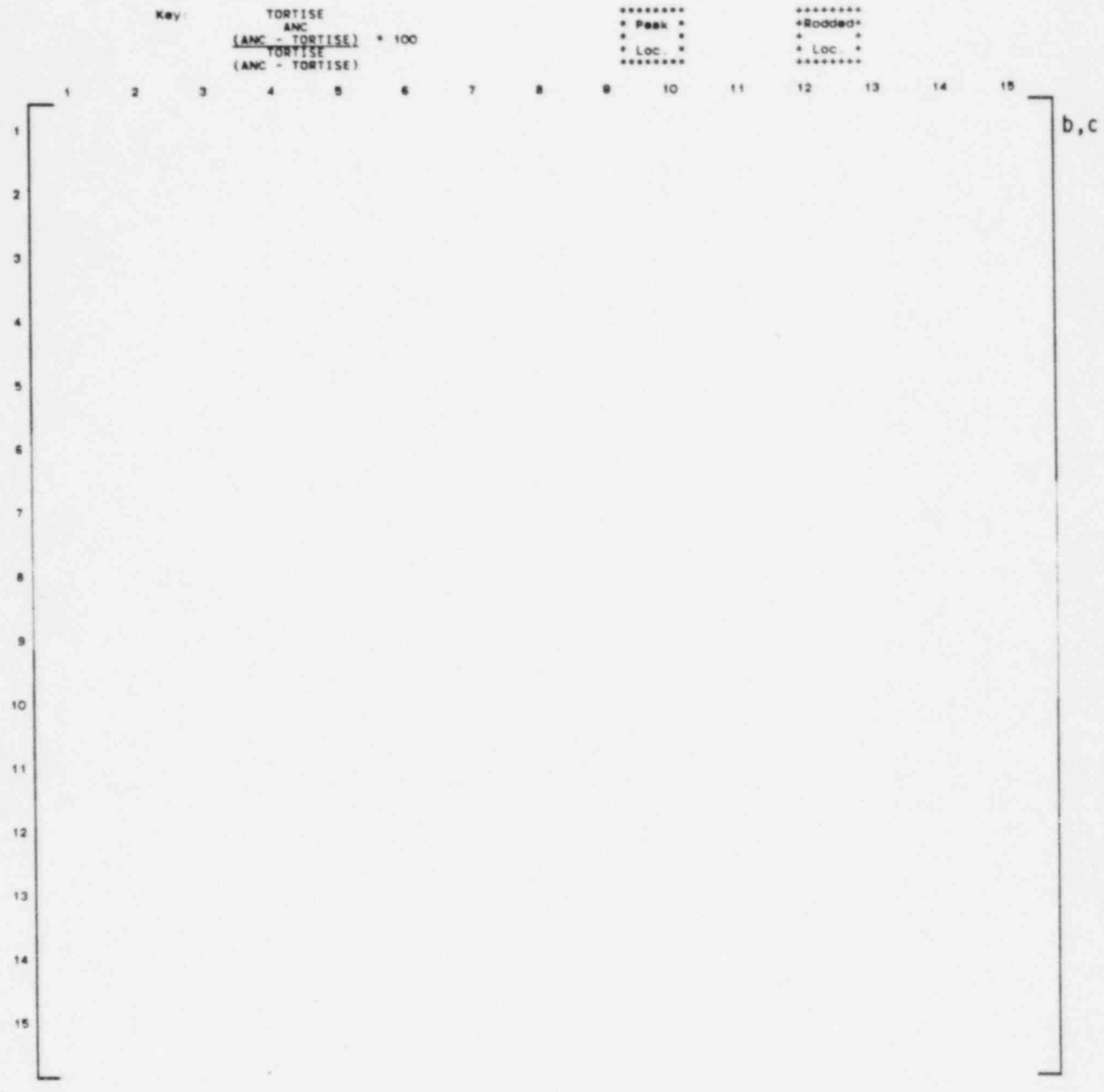

Figure 3-35. ANC/TORTISE Assembly Average Power Comparison
Plant C, Cycle 2, EOL, HZP
Off-Normal Operation -- Stuck Rod

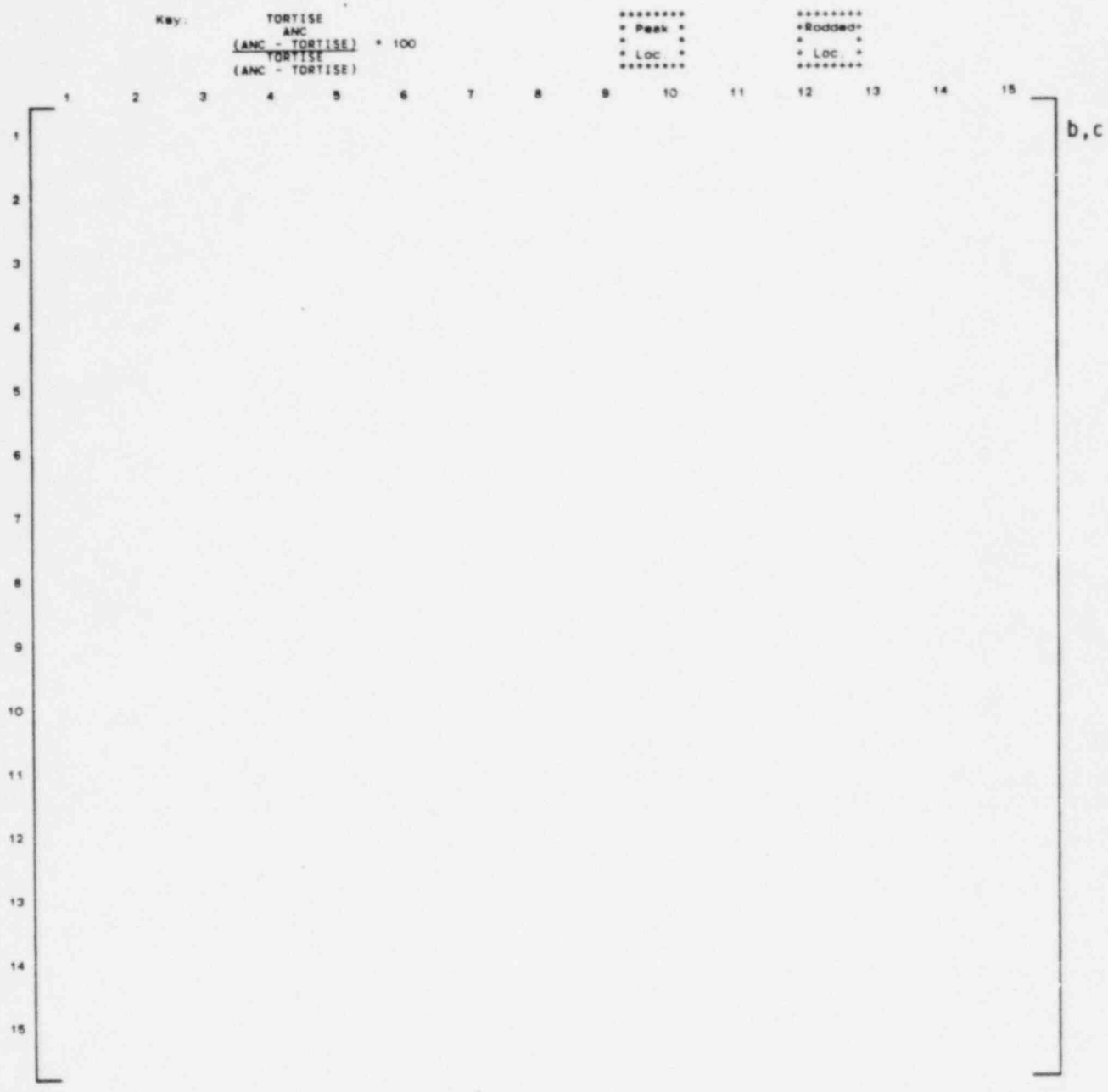

Figure 3-36. ANC/TORTISE Assembly Average Power Comparison
Plant C, Cycle 3, EOL, HZP
Off-Normal Operation -- Stuck Rod

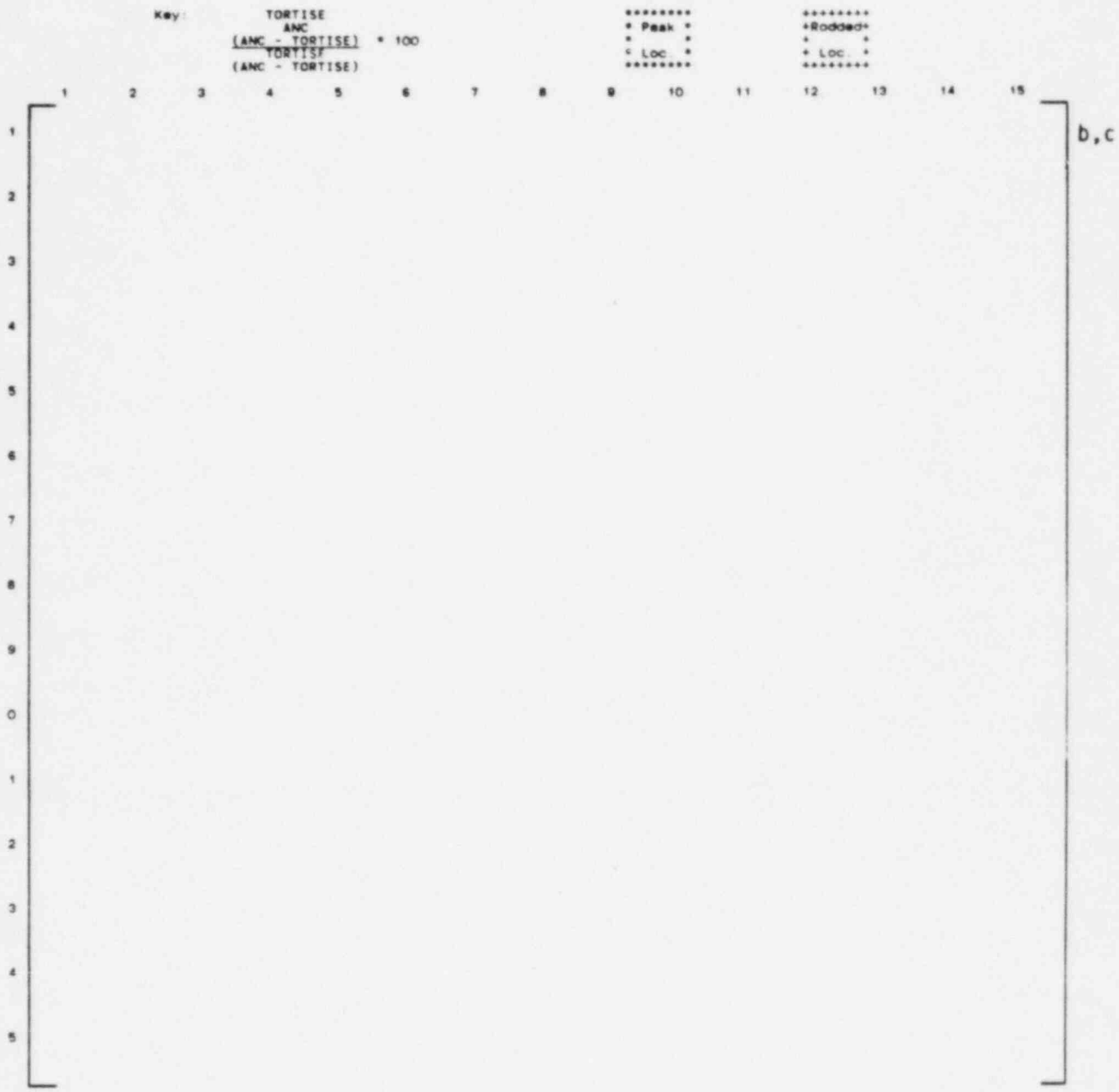

Figure 3-37. ANC/TORTISE Assembly Peak Power Comparison
Plant C, Cycle 2, EOL, HZP
Off-Normal Operation -- Stuck Rod

TABLE 3-16
SUMMARY OF ANC AND TORTISE CALCULATIONS
OFF-NORMAL OPERATION -- STUCK ROD

	Plant C Cycle 1	Plant C Cycle 2	Plant C Cycle 3	Mean	Standard Deviation
Condition	EOL HZP	EOL HZP	EOL HZP		
Rod Worth (pcm)	[				] b,c
TORTISE					
ANC					
Percent Difference					
Maximum Assembly Average Power					
TORTISE					
ANC					
Percent Difference					
Maximum Assembly Peak Power					
TORTISE					
ANC					
Percent Difference	]				

Figures and Tables for Subsection 3-2-3
Dropped Rod

TABLE 3-17
SUMMARY OF ANC AND TORTISE CALCULATIONS
OFF-NORMAL OPERATION -- DROPPED ROD

	Plant B Cycle 1	Plant C Cycle 1	Plant C Cycle 2	Plant C Cycle 3	Mean	Standard Deviation
Condition	BOL HFP	BOL HFP	BOL HFP	BOL HFP		
Rod Worth (pcm)	[					] b,c
TORTISE						
ANC						
Percent Difference						
Maximum Assembly Average Power						
TORTISE						
ANC						
Percent Difference						
Maximum Assembly Peak Power						
TORTISE						
ANC						
Percent Difference						]

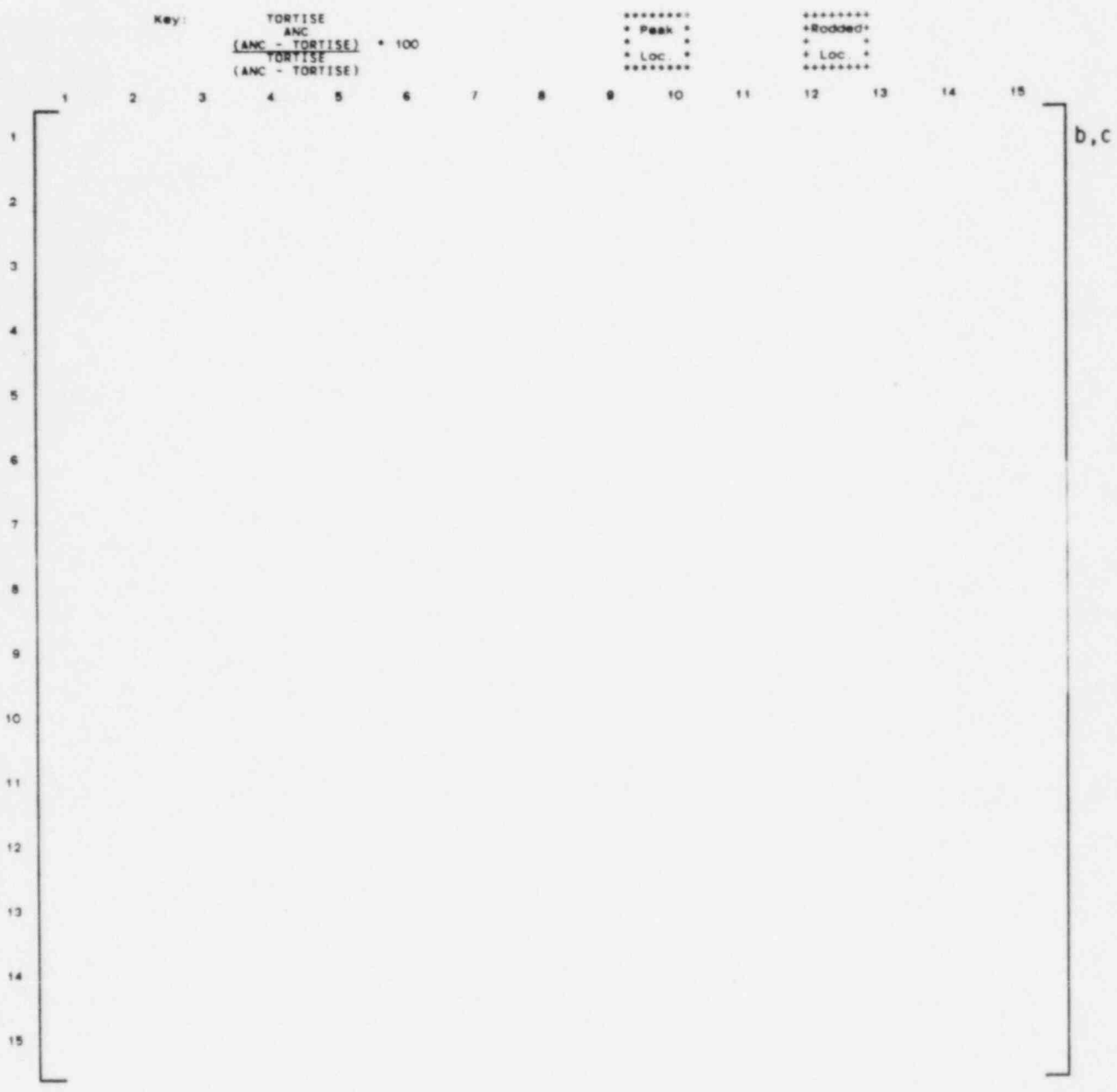

Figure 3-38. ANC/TORTISE Assembly Average Power Comparison
Plant B, Cycle 1, BOL, HZP
Off-Normal Operation -- Dropped Rod

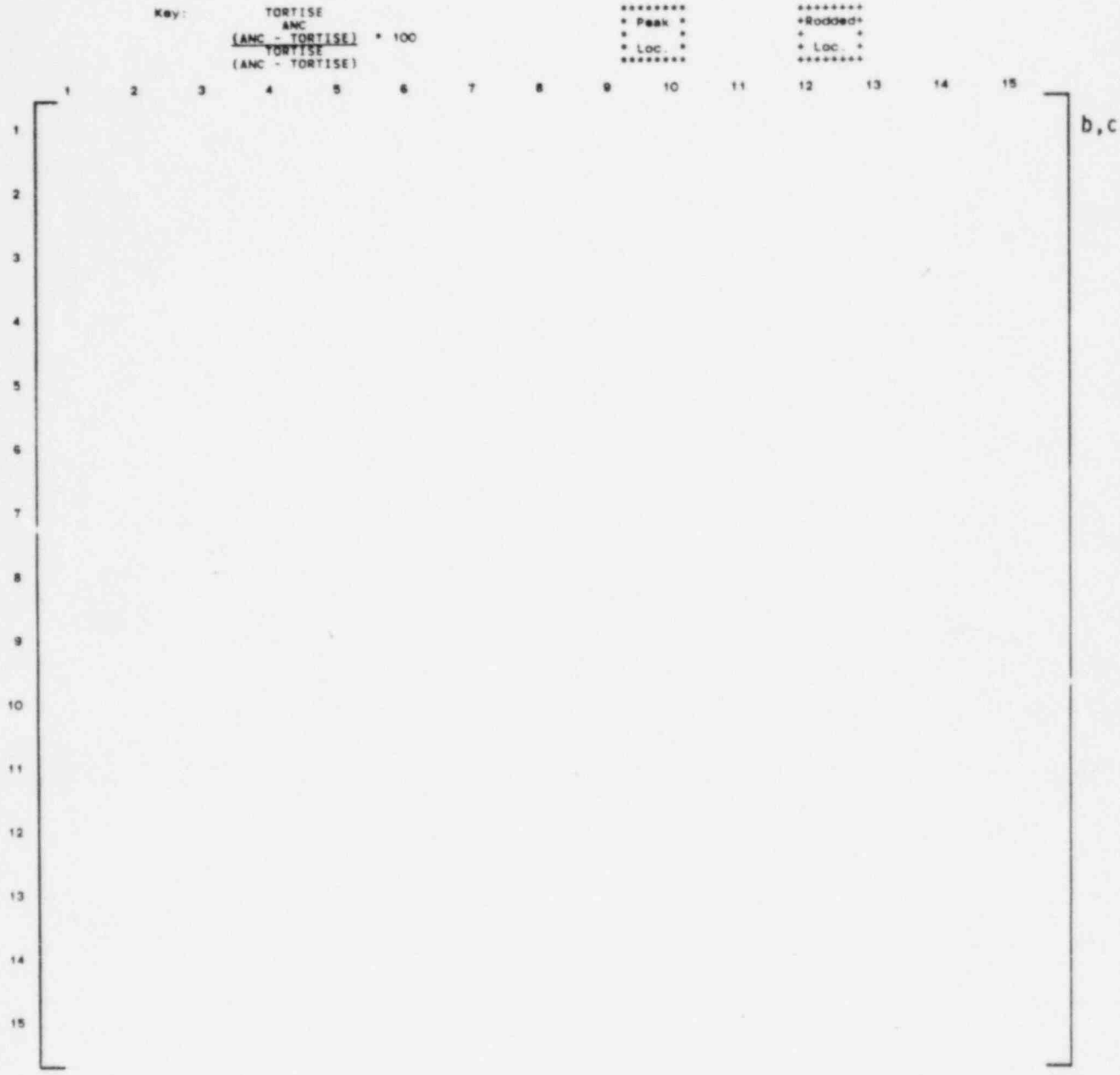

Figure 3-39. ANC/TORTISE Assembly Average Power Comparison
Plant C, Cycle 1, BOL, HZP
Off-Normal Operation -- Dropped Rod

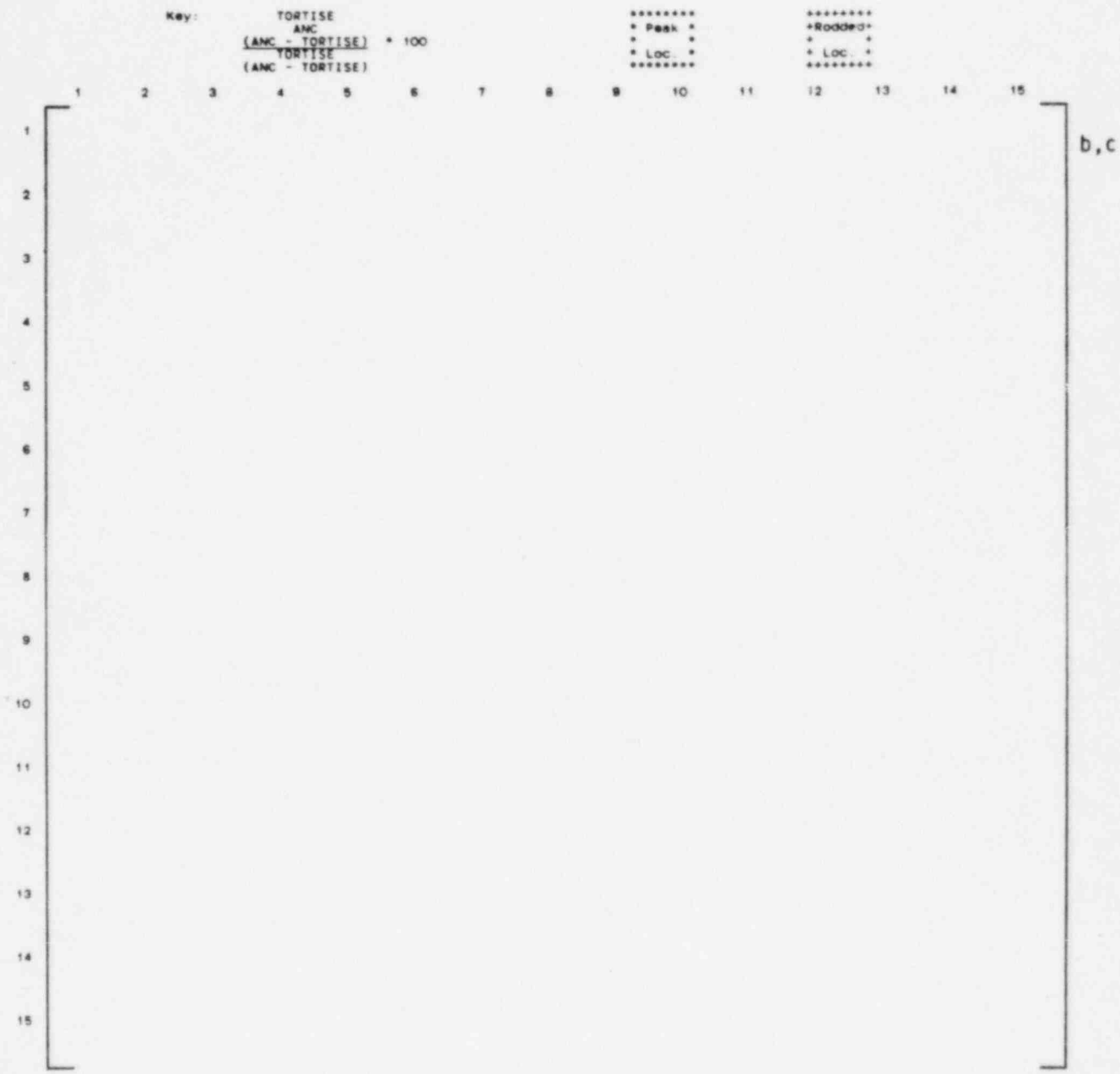

Figure 3-40. ANC/TORTISE Assembly Average Power Comparison
Plant C, Cycle 2, BOL, HFP
Off-Normal Operation -- Dropped Rod

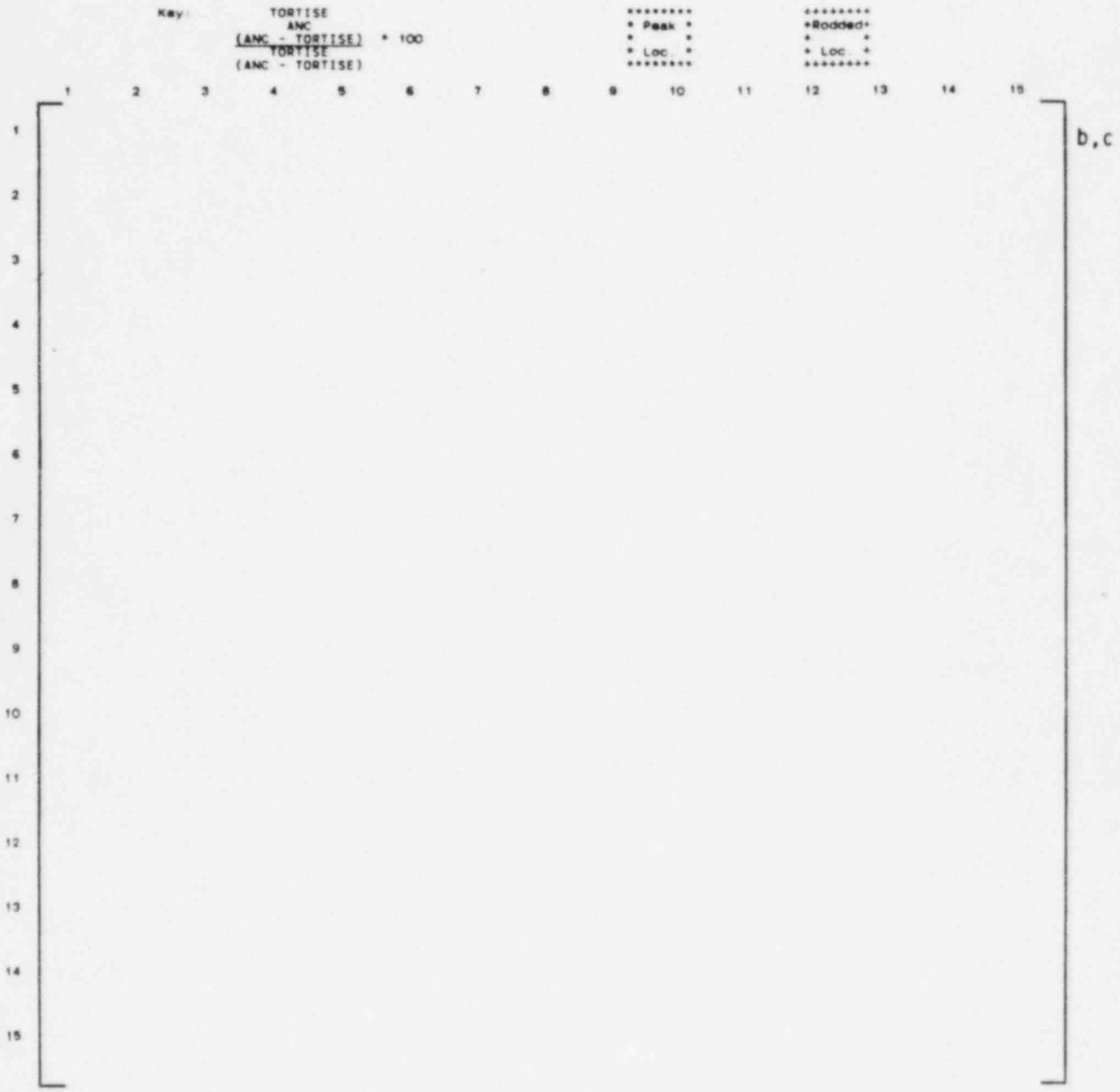

Figure 3-41. ANC/TORTISE Assembly Average Power Comparison
Plant C, Cycle 3, BOL, HFP
Off-Normal Operation -- Dropped Rod

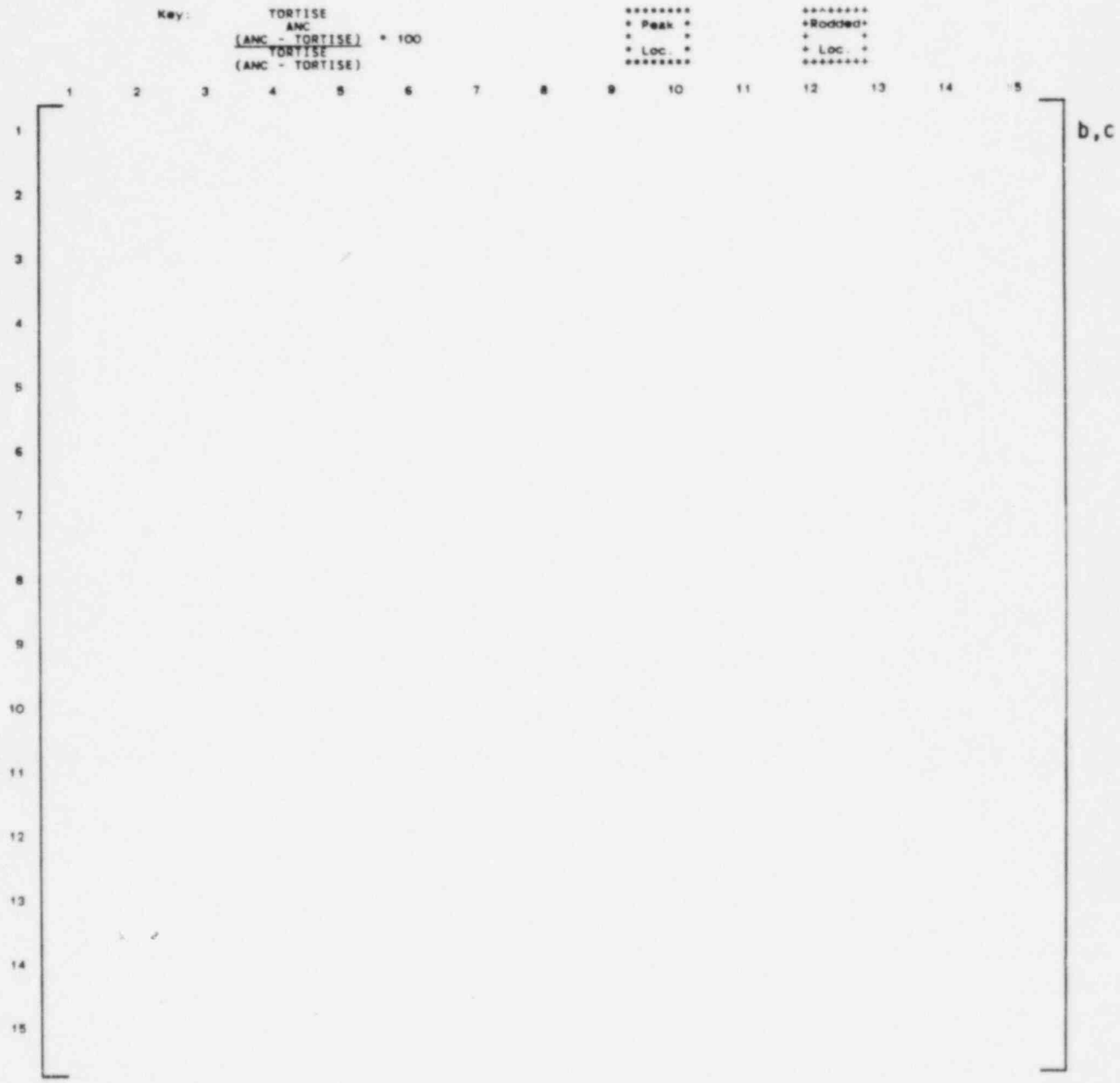

Figure 3-42. ANC/TORTISE Assembly Peak Power Comparison
Plant C, Cycle 2, BOL, HFP
Off-Normal Operation -- Dropped Rod

SECTION 4
CONCLUSIONS

Section 2 described the three components of the ANC methodology: the Nodal Expansion Method for the nodal equation solution, the group theory method for rod power recovery, and the equivalence theory for homogenization. Section 3 provided extensive comparisons of ANC with fine-mesh discrete TORTISE calculations and measurements to establish the accuracy of these models. These comparisons demonstrate that ANC predicts core reactivity, assembly average power, assembly peak rod power, and, it follows, all other core characteristics at both normal and off-normal conditions to the same level of accuracy as TORTISE predicts them.

For normal operation, the critical boron concentrations of ANC and TORTISE have a mean difference of [ ]^{b,c} ppm, with a standard deviation of [ ]^{b,c} ppm. The assembly average power and assembly peak rod power are also predicted with high accuracy. The mean difference in assembly average power between ANC and TORTISE is [ ]^{b,c} percent, with a standard deviation of [ ]^{b,c} percent. Assembly peak rod power differs by only [ ]^{b,c} percent, with a standard deviation of [ ]^{b,c} percent, between ANC and TORTISE. ANC predicts the maximum assembly peak rod power, or core peak power, on the average, with a difference of only [ ]^{b,c} percent, with a standard deviation of [ ]^{b,c} percent, from TORTISE. These results demonstrate a level of accuracy in ANC comparable to the discrete fine-mesh code. Integral parameters such as reactivity coefficients and control rod worths also compare favorably.

For off-normal conditions, the extreme power distributions are also predicted very accurately by ANC. ANC predictions for the core peak power for the ejected, stuck, and dropped control rod conditions differ, on the average, from TORTISE by [ ]^{b,c} percent, with a standard deviation of [ ]^{b,c} percent for the ejected rod condition; [ ]^{b,c} percent, with a standard deviation of [ ]^{b,c} percent for the stuck rod condition; and [ ]^{b,c} percent, with a standard deviation of [ ]^{b,c} percent for the dropped rod

condition. If all three conditions were grouped together, the average difference would be [ ]^{b,c} percent, with a standard deviation of [ ]^{b,c} percent, based on [ ]^{b,c} data points.

The results reported in section 3 demonstrate that ANC is an accurate analytical tool for multidimensional nuclear calculations performed in the design, safety analyses, and operational follow of pressurized water reactor cores. The intended usage of the Advanced Nodal Code encompasses all applications described in the reload safety evaluation methodology topical report.[3] Implementation of ANC will improve the quality of core physics predictions.

SECTION 5

REFERENCES

1. Camden, T. M., et al, "PALADON -- Westinghouse Nodal Computer Code," WCAP-9485A (proprietary) and WCAP-9486A (nonproprietary), December 1978.

2. Ankney, R. D., "PALADON -- Westinghouse Nodal Computer Code," WCAP-9485A, Supplement 1 (proprietary), and WCAP-9486A, Supplement 1 (nonproprietary), September 1981.

3. Bordelon, F. M., et al, "Westinghouse Reload Safety Evaluation Methodology," WCAP-9272 (proprietary) and WCAP-9273 (nonproprietary), March 1978.

4. Finnemann, H., Bennewitz, F., and Wagner, M. R., "Interface Current Techniques for Multidimensional Reactor Calculations," Atomkernergie 30, 123 (1977).

5. Makai, M. "Symmetries Applied to Reactor Calculations," Nuclear Science and Engineering, 82, 338--353 (1982).

6. Koebke, K., "Advances in Homogenization and Dehomogenization," ANS International Topical Meeting, Advances in Mathematical Methods for the Solution of Nuclear Engineering Problems, Volume 2, 59--73 (1981).

7. Altomare, S. and Barry, R. F., "The TURTLE 24.0 Diffusion Depletion Code," WCAP-7213 (proprietary), June 1968, and WCAP-7758 (nonproprietary), September 1971.

8. Argonne Code Center: Benchmark Problem Book, Argonne National Laboratory, ANL-7416, Supplement 2, 277--282 (1977).

9. Meyer, C. E. and Stover, R. L., "INCORE Power Distribution Determination in Westinghouse PWRs," WCAP-8498 (nonproprietary), July 1975.